



Filament Formation due to Diffusive Instabilities in Dusty Protoplanetary Disks

Konstantin Gerbig¹ , Min-Kai Lin (林明楷)^{2,3} , and Marius Lehmann² ¹ Department of Astronomy, Yale University, New Haven, CT 06511, USA; konstantin.gerbig@yale.edu² Institute of Astronomy and Astrophysics, Academia Sinica, Taipei 10617, Taiwan³ Physics Division, National Center for Theoretical Sciences, Taipei 10617, Taiwan

Received 2023 September 1; revised 2023 November 27; accepted 2023 November 28; published 2024 January 25

Abstract

We report the finding of a new, local diffusion instability in a protoplanetary disk which can operate in a dust fluid, subject to mass diffusion, shear viscosity, and dust–gas drag, provided the diffusivity, viscosity, or both, decrease sufficiently rapidly with increasing dust surface mass density. We devise a vertically averaged, axisymmetric hydrodynamic model to describe a dense, midplane dust layer in a protoplanetary disk. The gas is modeled as a passive component, imposing an effective, diffusion-dependent pressure, mass diffusivity, and viscosity onto the otherwise collisionless dust fluid, via turbulence excited by the gas alone, or dust and gas in combination. In particular, we argue that such conditions are met when the dust–gas mixture generates small-scale turbulence through the streaming instability, as supported by recent measurements of dust mass diffusion slopes in simulations. We hypothesize that the newly discovered instability may be the origin of filamentary features, almost ubiquitously found in simulations of the streaming instability. In addition, our model allows for growing oscillatory modes, which operate in a similar fashion as the axisymmetric viscous overstability in dense planetary rings. However, it remains speculative if the required conditions for such modes can be met in protoplanetary disks.

Unified Astronomy Thesaurus concepts: [Protoplanetary disks \(1300\)](#); [Planet formation \(1241\)](#); [Circumstellar dust \(236\)](#); [Hydrodynamics \(1963\)](#); [Astrophysical dust processes \(99\)](#); [Astrophysical fluid dynamics \(101\)](#)

1. Introduction

Protoplanetary disks are the birthplaces of planets. One key stage within the core-accretion scenario for planet formation involves the conversion of small dust particles into kilometer-sized planetesimals. The formation of planetesimals is associated with a multitude of challenges. Specifically, coagulation growth is thought to be inhibited at around meter sizes by both radial drift and the fragmentation of small solids (Birnstiel et al. 2012; Blum 2018).

For the last two decades, the attention has therefore been directed toward gravitational contraction of sufficiently massive disk regions, particle filaments, or local overdensities. Since the required dust-to-gas ratios are supersolar, one must invoke additional processes that can effectively concentrate dust particles. This includes secular gravitational instabilities (Ward 2000; Youdin 2011; Takahashi & Inutsuka 2014; Tominaga et al. 2019, 2020, 2023), particle traps such as pressure maxima (Onishi & Sekiya 2017; Shibaike & Alibert 2020; Xu & Bai 2022), turbulent concentration (Chambers 2010; Hartlep & Cuzzi 2020), and dust–gas drag instabilities (Johansen et al. 2015; Schäfer et al. 2017; Gerbig et al. 2020; Gerbig & Li 2023), the most prominent of which is the so-called streaming instability (Youdin & Goodman 2005; Jacquet et al. 2011; Squire & Hopkins 2018).

In its linear phase, the streaming instability utilizes the relative equilibrium velocity between dust and gas, in the classical picture induced by the background gas pressure gradient, to drive exponentially growing modes (Youdin & Goodman 2005). The streaming instability saturates, after a few dynamic timescales, into a quasi–steady state characterized by

turbulent particle density and velocity fluctuations (Johansen & Youdin 2007). Eventually, this system self-organizes into azimuthally elongated filaments which can drift inward and merge (see, e.g., Yang & Johansen 2014; Li et al. 2018; Li & Youdin 2021). The above three-step evolution has been readily observed in 3D shearing box simulations of both vertically stratified and unstratified protoplanetary disks where drag and dust feedback is included.

The formation of planetesimals within the streaming instability framework requires the additional component of dust self-gravity, which, albeit not a priori obvious, is thought to occur during the streaming instability’s nonlinear phase, either before or after the emergence of the overdense filaments. The nonlinear phase has been investigated numerically on numerous occasions. Specifically, Schreiber & Klahr (2018) found in 2D simulations that dust diffusivities tend to decrease with dust-to-gas ratio. This behavior was also seen in 3D, stratified simulations by Gerbig & Li (2023), and is typically attributed to the particles carrying too much collective inertia to be effectively diffused away by residual gas turbulence, and conversely, the back-reaction of the particles’ inertia onto the gas may lead to a decrease in diffusion with increasing dust-to-gas ratio. An alternative picture views particle diffusion similar to gas pressure (a model we aim to discuss thoroughly in this paper): a region of high diffusion expels particles toward regions of low diffusion.

Either way, the implication of particle diffusion decreasing with increasing dust density has hitherto not been investigated analytically in the context of the stability of dusty protoplanetary disks. The previous models by Chen & Lin (2020) and Umurhan et al. (2020) had diffusion depend on the stopping time and gas viscosity only, both of which are taken to be constant. In this paper, we perform an instability analysis of a sheet of particles subject to dust–gas drag forces and mass and momentum diffusion, where the diffusion coefficients are

allowed to vary with particle density. The existence of such a dependence has been established in hydrodynamic simulations by Schreiber & Klahr (2018) and Gerbig & Li (2023). Our treatment thus bears some similarity to hydrodynamic studies of the viscous instability (Lin & Bodenheimer 1981; Ward 1981; Salo & Schmidt 2010) and viscous overstability (Schmit & Tscharnuter 1995, 1999; Schmidt et al. 2001; Latter & Ogilvie 2009, 2010; Lehmann et al. 2017, 2019) in planetary rings.

This paper is structured as follows. We outline our hydrodynamical model, specifically focusing on the diffusion terms and their physical relevance, as well as perform a linear perturbation analysis, in Section 2. Next, we discuss the arising nonoscillatory and overstable modes in Sections 3 and 4, respectively. We discuss and contextualize our results in Section 5. Lastly, Section 6 concludes the paper with a summary of our findings.

2. Hydrodynamic Model

2.1. Diffusion and Viscosity In Particle-laden Protoplanetary Disks

Dust diffusion has long been identified to be of immense importance for dust dynamics and consequently planetesimal formation (see, e.g., Cuzzi et al. 1993). We deem it worth explicitly defining for this work the relevant property terms and putting them into the context of previous studies related to particle diffusion. For a recent comprehensive discussion on turbulent diffusion in protoplanetary disks we refer to Binkert (2023).

Generally speaking, diffusion acts to minimize free energy. In this work, we describe dust as a fluid subject to the diffusion of mass, driven by a gradient in dust concentration and momentum, driven by pressure gradients and shear stresses.

Under typical conditions, dust particles in protoplanetary disks are not collisional, and therefore do not experience collisional pressure forces. Instead, their dynamics are influenced by their coupling to the gas, namely via their stopping time t_s , which appears in the drag term of the momentum equation, i.e., $F_d \propto (\mathbf{v} - \mathbf{u})/t_s$, where \mathbf{v} and \mathbf{u} are particle and gas velocity, respectively. If the gas turbulence were fully characterized by the gas velocities \mathbf{u} , no additional diffusion terms would be needed in modeling dust diffusion in protoplanetary disks. Indeed, numerical simulations typically do not employ explicit diffusivity or viscosity, and instead compute diffusive effects indirectly via dust–gas interactions reflected in \mathbf{u} (e.g., Yang et al. 2018; Riols et al. 2020). As such a treatment is often not practical for analytical progress, we employ a diffusion subgrid model and describe diffusion and viscosity due to the particles’ coupling to the gas by using explicit terms in the hydrodynamical equations.

2.2. Governing Equations

Specifically, in this work, we will consider an isothermal, infinitesimally thin, axisymmetric particle disk in the absence of self-gravity, embedded in a gas that enters the system through diffusion, viscosity, and drag. In polar coordinates (r, ϕ) , the system is governed by the set of vertically averaged fluid equations

$$\frac{\partial \Sigma}{\partial t} + \frac{1}{r} \frac{\partial (r \Sigma v_r)}{\partial r} = \frac{1}{r} \frac{\partial}{\partial r} \left(r D \frac{\partial \Sigma}{\partial r} \right), \quad (1)$$

$$\frac{\partial v_r}{\partial t} + \left(v_r - \frac{D}{\Sigma} \frac{\partial \Sigma}{\partial r} \right) \frac{\partial v_r}{\partial r} = \frac{v_\phi^2}{r} - \Omega^2 r - \frac{v_r - u_r}{t_s} - \frac{1}{\Sigma} \frac{\partial (c_d^2 \Sigma)}{\partial r} + \frac{1}{\Sigma r} \frac{\partial}{\partial r} \left(r v_r D \frac{\partial \Sigma}{\partial r} \right) + F_r, \quad (2)$$

$$\frac{\partial v_\phi}{\partial t} + \left(v_r - \frac{D}{\Sigma} \frac{\partial \Sigma}{\partial r} \right) \frac{\partial v_\phi}{\partial r} = -\frac{v_\phi}{r} \left(v_r - \frac{D}{\Sigma} \frac{\partial \Sigma}{\partial r} \right) - \frac{v_\phi - u_\phi}{t_s} + F_\phi. \quad (3)$$

Equations (1) to (3) describe the dynamical evolution of the surface mass density Σ , the radial velocity v_r , and azimuthal velocity v_ϕ , respectively, where $\Omega = \sqrt{GM_*/r^3}$ is the Keplerian angular frequency, with stellar mass M_* and gravitational constant G . The continuity equation, Equation (1), takes the form of an advection–diffusion equation, with mass diffusivity for dust D . The momentum equations incorporate advection both by v_r and by the diffusion flux. This leads to the modified gradient advection terms on the left-hand sides of the momentum equations, as well as the modified curvature-related advection term on the right-hand side of Equation (3). In addition, the fifth term on the right-hand side of Equation (2) incorporates v_r advection of the momentum carried in the diffusion flux itself. We refer to Tominaga et al. (2019) for a discussion on these additional advection terms associated with the diffusion flux and their implications when the full dust–gas mixture is considered, but note that they allow the total gas and dust angular momentum to be conserved.

We provide a more rigorous justification for our set of hydrodynamical equations in Appendix A, using mean field theory based on Reynolds averaging and the application of a set of plausible closure relations. Given this context, the fields Σ and \mathbf{v} should be interpreted as mean fields separated in scale from the underlying small fluctuations that characterize turbulence.

Equation (2) includes the vertically averaged, effective dust pressure $P_d = \Sigma c_d^2$, with velocity dispersion c_d^2 of the dust fluid. Since the dust is assumed to be collisionless, this effective velocity dispersion is assumed to be generated solely by the particles’ coupling to the turbulence with $c_d^2 \propto D$. Specifically, we follow Klahr & Schreiber (2021) and Gerbig & Li (2023) and write

$$c_d^2 = \frac{D c_s^2}{t_s c_s^2 + D} \approx \frac{D}{t_s}, \quad (4)$$

which follows from a balance between diffusion and sedimentation. The latter approximation requires $D \ll t_s c_s^2$, which is the case in numerical simulations (e.g., Schreiber & Klahr 2018; Gerbig & Li 2023). We discuss this pressure model in Appendix B.

Finally, we include explicit momentum diffusion terms, modeled by Navier–Stokes stress terms F_r and F_ϕ . They can be calculated via

$$\mathbf{F} = \frac{1}{\Sigma} \nabla \cdot \mathbf{T}, \quad (5)$$

with viscous stress tensor T , the components of which are

$$T_{ij} = \nu \Sigma \left(\frac{\partial v_i}{\partial x_j} + \frac{\partial v_j}{\partial x_i} - \frac{2}{3} \delta_{ij} \nabla \cdot \mathbf{v} \right), \quad (6)$$

where ν is the effective vertically averaged, kinematic, shear viscosity of the particle fluid. The inclusion of these shear stress terms differentiates Equations (2) and (3) from the dust momentum equations used by Tominaga et al. (2019). Our model also distinguishes itself from other works concerning dusty protoplanetary disks on the scales of planetesimal formation as we consider diffusivity D and viscosity ν , and consequently via Equation (4), the velocity dispersion c_d and dust pressure, to depend on surface mass density Σ . Specifically, we assert power-law dependencies of the form

$$D \propto \left(\frac{\Sigma}{\Sigma_0} \right)^{\beta_{\text{diff}}}, \quad (7)$$

$$\nu \propto \left(\frac{\Sigma}{\Sigma_0} \right)^{\beta_{\text{visc}}}, \quad (8)$$

where β_{diff} and β_{visc} are dimensionless exponents. We also introduce the corresponding dimensional slopes

$$\beta_D = \frac{\partial(D\Sigma)}{\partial\Sigma} = D(1 + \beta_{\text{diff}}), \quad (9)$$

$$\beta_\nu = \frac{\partial(\nu\Sigma)}{\partial\Sigma} = \nu(1 + \beta_{\text{visc}}). \quad (10)$$

At high dust-to-gas ratios, β_D has been found to be negative (Schreiber & Klahr 2018; Gerbig & Li 2023). We are not aware of any numerical constraints on β_ν within the context of turbulent diffusion in dusty protoplanetary disks.

2.3. Model Applicability

Equations (1)–(3) can be applied if the combined inertia of the disk is dominated by the particle fluid, for dust-to-gas volume mass density ratios $\rho_p/\rho_g \gtrsim 1$. In this case, the presence of the gas can be reduced to perturbations that evoke drag, mass diffusion, and momentum diffusion (aka viscosity). While the analytic model itself is agnostic to the source of diffusion and viscosity, in this paper, we specifically apply it to particle layers in the midplane of the protoplanetary disk, subject to the nonlinear streaming instability.

Given this context, our model is restricted to radial length scales exceeding the characteristic scale of the underlying turbulence, in this case, the characteristic scale of the streaming instability, which for $\tau_s \sim 1$, is $l_{\text{SI}} \sim \eta r$ (e.g., Youdin & Goodman 2005; Squire & Hopkins 2018; Gerbig et al. 2020), where $\eta \sim 0.01$ characterizes the radial pressure gradient in the disk, and thus scales with the equilibrium relative velocity between the dust and gas. For smaller stopping times, this restriction is relaxed, as the characteristic scale of the linear streaming instability decreases (e.g., Lin & Youdin 2017, Appendix D). Also note that in the vertical direction, this restriction is formally always satisfied as our model is vertically unstratified, implying a vanishing vertical wavenumber of all modes. Whether or not such modes are supported by an actual vertically stratified dust layer requires a stratified analysis and is thus subject to future work.

We further point out that a fluid description for particles in protoplanetary disks, as applied here, is strictly only valid if $t_s < \Omega^{-1}$, since for decoupled grains the dynamical evolution of the stress tensor cannot, in general, be ignored (see, e.g., Garaud et al. 2004; Jacquet et al. 2011), and must be modeled using a kinetic approach. In this work, we instead assume that the “external” turbulence is able to establish a simple Newtonian stress–strain relation for the particle fluid, characterized by the shear viscosity ν and isotropic velocity dispersion c_d , as discussed in Section 2.2 and Appendix A. This is to some extent similar to the effect of mutual particle collisions in planetary rings, which indeed, if frequent enough, are known to establish a Newtonian stress–strain relation of the particle flow (e.g., Stewart et al. 1984; Shu & Stewart 1985). However, streaming instability turbulence, which is the main application of our model, is not expected to occur for large stopping times, which withdraws the physical justification for this assumption (at least given this context). In addition, mutual collisions, which are ignored in our model, may in principle become relevant if the velocity dispersion $c_d \propto t_s^{-1/2}$ becomes sufficiently small.

Despite these limitations, we will also present and discuss results assuming larger particles with $t_s > \Omega^{-1}$. In doing so, we retain a concrete connection to the viscous instability and overstability in planetary rings. Also, if large grains in protoplanetary disks do experience momentum and mass diffusion by some means (see the discussion in Section 5.5), our model may still provide useful insights, despite lacking the stress tensor evolution contained in a kinetic approach.

2.4. Linearized Equations and Dispersion Relation

We adopt a local, corotating Cartesian reference frame at distance R from the star such that $(x, y) = (r - R, R(\phi - \Omega t))$ and $v_x = v_r$, $v_y = v_\phi - R\Omega$. We then perturb the system around a background state such that $\Sigma = \Sigma_0 + \Sigma'$, $v_x = v'_x$, $v_y = -q\Omega x + v'_y$ with $\Sigma_0 = \text{const.}$, and linearize in perturbed quantities. Following Appendix B in Klahr & Schreiber (2021), we neglect the perturbed gas velocity \mathbf{u}' such that the linearized drag terms are $\propto -\mathbf{v}'/t_s$, which is justified if the mean field quantities derived in Appendix A are time averaged over one turbulent correlation time. This assumption conveniently decouples the dust and gas equations and allows us to isolate the effects of dust density–dependent turbulence alone.

For Keplerian shear where $q = 3/2$, Equations (1)–(3) thus become

$$\frac{1}{\Sigma_0} \frac{\partial \Sigma'}{\partial t} + \frac{\partial v'_x}{\partial x} = \frac{1}{\Sigma_0} \frac{\partial}{\partial x} \left(D \frac{\partial \Sigma'}{\partial x} \right), \quad (11)$$

$$\begin{aligned} \frac{\partial v'_x}{\partial t} - 2\Omega v'_y &= -\frac{v'_x}{t_s} \\ &\quad - \frac{1}{\Sigma_0 t_s} \frac{\partial(D\Sigma)}{\partial\Sigma} \frac{\partial \Sigma'}{\partial x} + \nu \frac{4}{3} \frac{\partial^2 v'_x}{\partial x^2}, \end{aligned} \quad (12)$$

$$\begin{aligned} \frac{\partial v'_y}{\partial t} + \frac{\Omega v'_x}{2} &= -\frac{v'_y}{t_s} - \frac{\Omega}{2} \frac{D}{\Sigma_0} \frac{\partial \Sigma'}{\partial x} \\ &\quad + \nu \frac{\partial^2 v'_y}{\partial x^2} - \frac{3\Omega}{2\Sigma_0} \frac{\partial(\nu\Sigma)}{\partial\Sigma} \frac{\partial \Sigma'}{\partial x}. \end{aligned} \quad (13)$$

This set of linearized equations is novel in that it includes a Navier–Stokes viscosity for the particle fluid; relates the

particle pressure to the diffusion and stopping time via Equation (4), which produces the second term on the r.h.s. of the radial momentum equation; and takes into account the dependence of diffusion and viscosity on the particle surface mass density, as motivated by the simulations of Schreiber & Klahr (2018) and Gerbig & Li (2023). As a consequence, the radial and azimuthal momentum equations respectively contain the slope of the diffusion and viscosity with respect to the particle surface mass density. Depending on the slope, these terms can act by both stabilizing or destabilizing on perturbations to the equilibrium state defined above, as we discuss below. The mass diffusion term in the continuity equation, the terms $\propto \partial/\partial x^2$ (assuming $\nu > 0$), and the term describing advection of background shear by the diffusion flux (second term on right-hand side of Equation (3)) are always stabilizing. Note, that this diffusion flux term is the only term from the four angular momentum conserving terms in Equations (2) and (3) added by Tominaga et al. (2019) that survives linearization. Notably, it behaves like the fourth term on the right-hand side of Equation (13) containing the viscosity gradient. For the rest of the paper, “diffusion flux” references this term specifically unless stated otherwise. Lastly, the drag terms have a stabilizing effect. In our analysis, we include both radial and azimuthal drag terms, which is in contrast to Klahr & Schreiber (2021) who drop the azimuthal drag term.

We proceed by introducing axisymmetric modes of the form

$$f' = \Re(\hat{f} e^{-ikx+nt}), \quad (14)$$

with complex frequency n and (radial) wavenumber k . We take $k > 0$ without loss of generality. Modes grow and decay for $\Re(n) > 0$ and $\Re(n) < 0$, respectively, and $\Im(n)$ corresponds to the oscillation frequency, the sign of which sets the wave travel direction. We get

$$n \frac{\hat{\Sigma}}{\Sigma_0} = ik\hat{v}_x - Dk^2 \frac{\hat{\Sigma}}{\Sigma_0}, \quad (15)$$

$$n\hat{v}_x - 2\Omega\hat{v}_y = -\frac{\hat{v}_x}{t_s} + \frac{ik}{t_s}\beta_D \frac{\hat{\Sigma}}{\Sigma_0} - \frac{4}{3}\nu k^2 \hat{v}_x, \quad (16)$$

$$n\hat{v}_y + \frac{\Omega}{2}\hat{v}_x = -\frac{\hat{v}_y}{t_s} + \frac{ik}{2}D\Omega \frac{\hat{\Sigma}}{\Sigma_0} - \nu k^2 \hat{v}_y + \frac{3}{2}ik\Omega\beta_\nu \frac{\hat{\Sigma}}{\Sigma_0}. \quad (17)$$

This system is solved by a cubic dispersion relation of the form

$$n^3 + n^2 a_2 + n a_1 + a_0 = 0, \quad (18)$$

with coefficients

$$a_2 = \left(\frac{7}{3}\nu + D\right)k^2 + \frac{2}{t_s}, \quad (19)$$

$$a_1 = \left(\frac{7}{3}D\nu + \frac{4}{3}\nu^2\right)k^4 + \left(\frac{2D}{t_s} + \frac{7}{3}\frac{\nu}{t_s} + \frac{\beta_D}{t_s}\right)k^2 + \frac{1}{t_s^2} + \Omega^2, \quad (20)$$

$$a_0 = \left(\frac{4}{3}D\nu^2\right)k^6 + \left(\frac{7}{3}\frac{D\nu}{t_s} + \frac{\nu}{t_s}\beta_D\right)k^4 + \left(2D\Omega^2 + \frac{D}{t_s^2} + \frac{\beta_D}{t_s^2} + 3\Omega^2\beta_\nu\right)k^2. \quad (21)$$

2.5. Dimensionless Quantities

It is convenient to write the dispersion relation in terms of commonly used dimensionless quantities. The orbital frequency introduces a time unit, such that we write the dimensionless stopping time as

$$\tau_s \equiv t_s \Omega, \quad (22)$$

which, in general, is distinct from the so-called Stokes number defined as the ratio of the stopping time and turbulent correlation time (also known as the eddy time or integral time; Cuzzi et al. 1993; Youdin & Lithwick 2007). Particles with $\tau_s \ll 1$ are well coupled to the gas while $\tau_s \gg 1$ applies to loosely coupled dust.

Our reference length unit is the gas pressure scale height, which is the ratio of the (gas) sound speed c_s and orbital frequency, $H = c_s/\Omega$. We write the dimensionless wavenumber as $K \equiv kH$. Dimensionless versions of the ground state diffusivity in Equation (7) and viscosity in Equation (8) are introduced as

$$\delta \equiv \frac{D}{c_s H}, \quad (23)$$

$$\alpha \equiv \frac{\nu}{c_s H}, \quad (24)$$

where we use the same nomenclature as the well-known Shakura–Sunyaev α -parameter (Shakura & Sunyaev 1973), albeit in our work, α describes the effective viscosity of the dust fluid, and not the viscosity of the gas that is often adopted to model angular momentum transport in protoplanetary disks. The corresponding power-law slopes of the diffusivity and viscosity were defined in Equations (7) and (8), i.e., $\beta_{\text{diff}} = \partial \ln \delta / \partial \ln \Sigma$ and $\beta_{\text{visc}} = \partial \ln \alpha / \partial \ln \Sigma$, respectively. Typical values for the diffusivity and its slope are $10^{-5} \lesssim \delta \lesssim 10^{-4}$ and $-3 \lesssim \beta_{\text{diff}} \lesssim -1$, respectively, at high dust-to-gas ratios (Schreiber & Klahr 2018; Gerbig & Li 2023). Appropriate constraints on the particle viscosity α are less clear. In resistive simulations of the magneto-rotational instability (Balbus & Hawley 1991), Yang et al. (2018) measured a shear viscosity of $\alpha \sim 10^{-4}$ in the gas. However, that value includes (albeit presumably small) contributions from Maxwell stresses, and constitutes an average value throughout the particle layer. We are not aware of any other applicable constraints on α in the particle layer, or any measurements of β_{visc} .

We define the hydrodynamic Schmidt number as the ratio of the viscosity and mass diffusion coefficient for our particle fluid, i.e.,

$$\text{Sc} \equiv \frac{\alpha}{\delta}, \quad (25)$$

which is analogous to the definition used for pure gas in protoplanetary disks by Johansen & Klahr (2005) and Carballido et al. (2006). As pointed out in Youdin & Lithwick (2007), in the context of particles in protoplanetary disks, the Schmidt

number suffers from being oversubscribed, as it is also used to describe the ratio of the gas viscosity to particle diffusivity (Cuzzi et al. 1993; Schreiber & Klahr 2018; Binkert 2023). Here, we are primarily interested in the dust component, hence we assign Sc to characterize the relative importance of particle viscosity and particle diffusivity, both of which stem from the particles' coupling to gas turbulence.

Lastly, we notice that for $\delta > 0$, the dispersion relation includes a degeneracy in wavenumber and diffusivity, such that we can define

$$\xi \equiv \delta K^2 = \frac{Dk^2}{\Omega}. \quad (26)$$

Note, that since the herein utilized description for dust pressure is only appropriate for $\tau_s \gg \delta$, we equivalently require $\xi \ll \tau_s K^2$. As noted in Section 2.3, our model is only appropriate for scales larger than the scale of the underlying turbulence. We thus require $\xi \lesssim 4\pi^2 \delta / ((H/r)^2 \eta^2)$. For typical values of $H/r = 0.1$, $\eta \sim 1\%$, and for fiducial diffusivities of $\delta \sim 10^{-5} - 10^{-4}$, this corresponds to a maximum ξ of order unity. This is why, for the remainder of this study, we will mostly be concerned with the long-wavelength limit where $\xi < 1$.

The dimensionless complex frequency is denoted as

$$\sigma \equiv \frac{n}{\Omega} \equiv \gamma + i\omega, \quad (27)$$

where $\gamma = \Re(\sigma)$ is the growth rate and $\omega = \Im(\sigma)$ is the oscillation frequency. The dimensionless version of the cubic dispersion relation in Equation (18) is given by

$$\sigma^3 + \sigma^2 A_2 + \sigma A_1 + A_0 = 0, \quad (28)$$

with

$$A_2 = \left(\frac{7}{3}Sc + 1\right)\xi + \frac{2}{\tau_s}, \quad (29)$$

$$A_1 = \frac{Sc}{3}(7 + 4Sc)\xi^2 + \left(\frac{7}{3}Sc + 3 + \beta_{\text{diff}}\right)\frac{\xi}{\tau_s} + \frac{1}{\tau_s^2} + 1, \quad (30)$$

$$A_0 = \frac{4}{3}Sc^2\xi^3 + \frac{Sc}{\tau_s}\left(\frac{10}{3} + \beta_{\text{diff}}\right)\xi^2 + \left[2 + \frac{1}{\tau_s^2}(2 + \beta_{\text{diff}}) + 3Sc(1 + \beta_{\text{visc}})\right]\xi, \quad (31)$$

where A_0 , A_1 , and A_2 are real coefficients. This implies that $A_0 < 0$ is a sufficient condition for a nonoscillatory instability, as then there is at least one real positive root of Equation (28). The full, complex dispersion relation can also be cast into two equations for the growth rate and oscillation frequency, which need to hold independently

$$\omega^3 - 3\omega\gamma^2 - 2\omega\gamma A_2 - \omega A_1 = 0, \quad (32)$$

$$\gamma^3 - 3\omega^2\gamma - \omega^2 A_2 + \gamma^2 A_2 + \gamma A_1 + A_0 = 0. \quad (33)$$

3. Diffusive Instability

This section investigates the diffusive instability associated with the real roots of the dispersion relation in Equation (28).

Consider, however, first the case with zero diffusivity and viscosity, i.e., $Sc = 0$, $\xi = 0$. In this limit, the above dispersion relation reduces to

$$\sigma \left(\sigma^2 + \frac{2}{\tau_s}\sigma + \frac{1}{\tau_s^2} + 1 \right) = 0, \quad (34)$$

which is solved by damped, epicyclic waves with oscillation frequency Ω and negative growth rate $-t_s^{-1}$. The purely real root is the static null solution with $\sigma = \gamma = \omega = 0$. It is this mode that will get destabilized by diffusion and/or viscosity, as we discuss in the following. As this section is only concerned with the nonoscillatory, purely real solution, we set $\omega = 0$, and replace $\sigma = \gamma$. We will redirect our attention to oscillatory modes in Section 4.

3.1. Inviscid Case

We first investigate the purely diffusive case, where $Sc = 0$. In this limit the dispersion relation can be written as

$$\begin{aligned} \gamma^3 + \left(\xi + \frac{2}{\tau_s}\right)\gamma^2 &+ \left[(3 + \beta_{\text{diff}})\frac{\xi}{\tau_s} + \frac{1}{\tau_s^2} + 1 \right]\gamma \\ &+ \xi \left[2 + \frac{1}{\tau_s^2}(2 + \beta_{\text{diff}}) \right] = 0, \end{aligned} \quad (35)$$

which leads to unconditional instability if

$$\beta_{\text{diff}} < -2 - 2\tau_s^2. \quad (36)$$

For realistic power-law slopes of $\beta_{\text{diff}} \gtrsim -3$ (Schreiber & Klahr 2018; Gerbig & Li 2023), inviscid ($Sc = 0$) diffusive instability thus requires $\tau_s \lesssim 1$.

For small growth rates $\gamma \ll 1$, we find from Equation (35),

$$\gamma \simeq -\frac{\xi[2 + \tau_s^{-2}(2 + \beta_{\text{diff}})]}{1 + \tau_s^{-2} + \xi\tau_s^{-1}(3 + \beta_{\text{diff}})}, \quad (37)$$

which for small stopping times equals

$$\gamma \simeq -\xi(2 + \beta_{\text{diff}}) \quad (\tau_s \ll 1). \quad (38)$$

Figure 1 shows the growth rate for the inviscid diffusive instability for choices of the slope β_{diff} and stopping time τ_s for modes with $\xi = 0.1$, which for a fiducial $\delta = 10^{-5}$ corresponds to $K = 100$. Note that instability requires $\beta_{\text{diff}} < -2$, which is consistent with the more general condition in Equation (36) in the limit $\tau_s \ll 1$.

Figure 2 shows the growth rates of the inviscid diffusive instability for $\beta_{\text{diff}} = -3$ for various stopping times. The system is either stable (for $\tau_s \gtrsim 1$) or unstable (for $\tau_s \lesssim 1$) for all ξ . In fact, we note that inviscid diffusive instability is not damped at small scales, but displays the fastest growth rates at scales $\xi > 1$, which is where our model breaks down, as indicated by the hatched region in Figure 2.

The physical origin of the inviscid diffusive instability lies in the dust pressure term in Equation (2). For $\beta_{\text{diff}} < 0$, this pressure term acts by destabilizing and accelerating particles toward annuli of high density and low diffusivity. If β_{diff} is sufficiently steep for Equation (36) to hold, i.e., $\beta_{\text{diff}} < -2 - 2\tau_s^2$, this pressure forcing can overcome the

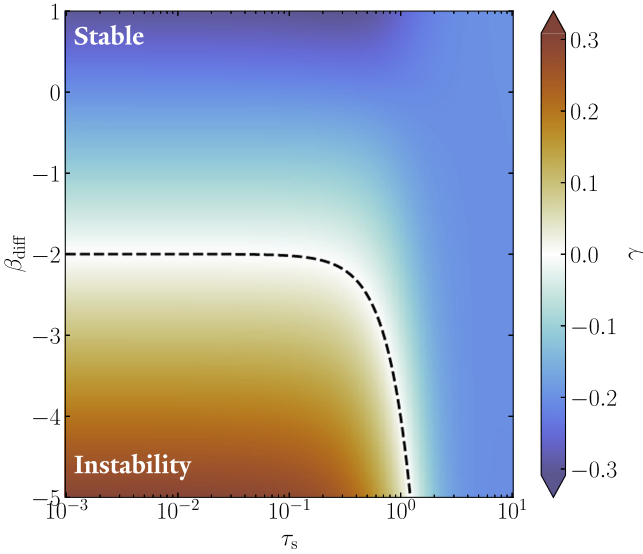


Figure 1. Growth rates for the inviscid ($Sc = 0$) diffusive instability driven by the diffusion-dependent pressure for $\xi = 0.1$. The black dashed line corresponds to Equation (36), below which the instability can operate, and above which, perturbations are exponentially damped.

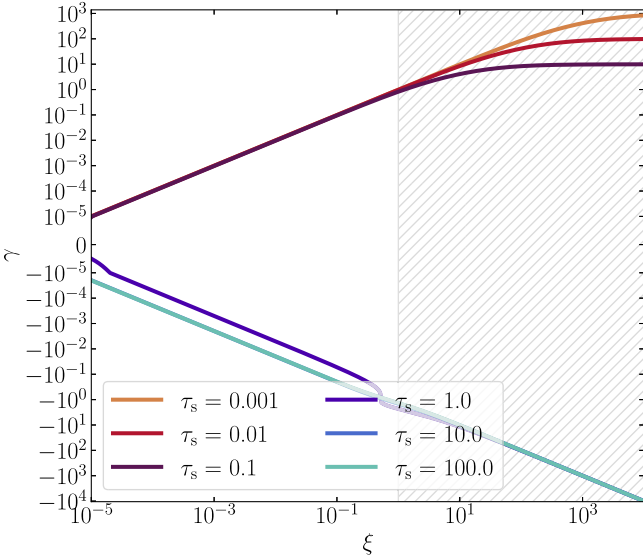


Figure 2. Growth rates for the inviscid ($Sc = 0$) diffusive instability driven by the diffusion-dependent pressure for $\beta_{\text{diff}} = -3$ and various stopping times. The hatched region corresponds to $\xi > 1$, for which our model ceases to be appropriate. The lines for $\tau_s = 10$ and $\tau_s = 100$ overlap.

stabilizing mass diffusion term in Equation (1) and the drag terms in the momentum equations. This increases the density, while in the process further decreasing diffusion, resulting in positive feedback and instability. In the large stopping time limit, the drag terms vanishes, as too does the destabilizing pressure term. The only remaining terms are the mass diffusion term in the continuity equation, and the diffusion flux term in Equation (13), both of which act to repel particles away from density maxima. Hence, the onset of this instability requires that stopping times are small.

3.2. $Sc = 1$ case

Next, we consider the case where $D = \nu$, equivalently $Sc = 1$, such that the equilibrium value of momentum diffusion

equals that of the mass diffusion, and also the power-law slopes of the diffusion and viscosity are identical, i.e., $\beta_{\text{visc}} = \beta_{\text{diff}}$. Under these assumptions, the dispersion relation is

$$\begin{aligned} & \gamma^3 + \left(\frac{10}{3}\xi + \frac{2}{\tau_s} \right) \gamma^2 \\ & + \left[\frac{11}{3}\xi^2 + \left(\frac{16}{3} + \beta_{\text{diff}} \right) \frac{\xi}{\tau_s} + \frac{1}{\tau_s^2} + 1 \right] \gamma \\ & + \frac{4}{3}\xi^3 + \left(\frac{10}{3} + \beta_{\text{diff}} \right) \frac{\xi^2}{\tau_s} \\ & + \left[5 + \frac{2}{\tau_s^2} + \left(3 + \frac{1}{\tau_s^2} \right) \beta_{\text{diff}} \right] \xi = 0. \end{aligned} \quad (39)$$

Pure instability is achieved if

$$\beta_{\text{diff}} < -\frac{4\xi^2\tau_s^2 + 10\xi\tau_s + 15\tau_s^2 + 6}{3\xi\tau_s + 9\tau_s^2 + 3}. \quad (40)$$

In the long-wavelength limit of $\xi < 1$, we recover our finding for the inviscid case where a power-law gradient $\beta_{\text{diff}} < -2$ suffices for instability if the stopping times are sufficiently small: $\tau_s \ll 1$. This is because for small stopping times and at large radial length scales, the destabilizing pressure term dominates over the viscosity terms.

For large stopping times of $\tau_s \gg 1$, the explicit drag terms and the pressure term become negligible. In this case, the long-wavelength limit $\xi < 1$ yields

$$\beta_{\text{diff}} \lesssim -\frac{(4\xi^2 + 15)\tau_s + 10\xi}{9\tau_s + 3\xi} \approx -\frac{5}{3}. \quad (41)$$

The diffusive instability behaves now analogously to the classical viscous instability (Ward 1981; Lin & Bodenheimer 1981), in that the instability is driven by the density slope of the shear viscosity that appears in the azimuthal momentum equation (Equation (13)). If the slope is sufficiently steep, there is a net flux toward density maxima that amplifies the linear perturbation. The criterion for the classical viscous instability is given by $\beta_{\text{visc}} < -1$. Our modification in Equation (41) is due to the inclusion of the mass diffusion term in the continuity equation (Equation (11)) and the diffusion flux in Equation (13). Both of these terms are always stabilizing, and hence the required viscosity slope for diffusive instability driven by viscosity that operates in the $\tau_s \gg 1$ limit is steeper than in the classical case.

It is easy to see in Equation (31) that if $\tau_s \ll 1$, the slope of the mass diffusion will dominate, whereas for $\tau_s \gg 1$, the slope of the momentum diffusion will dominate, thus leading to diffusive instability driven by the pressure term and viscosity terms, respectively. For marginally coupled particles $\tau_s \sim 1$, the instability can utilize both slopes. Because of this, on large scales $\xi \lesssim 1$, if β_{diff} is sufficiently negative, the system is unstable regardless of the stopping time.

For small growth rates $\gamma \ll 1$, and for small ξ , the real root of Equation (39) behaves as

$$\gamma \simeq -\frac{[5 + 2\tau_s^{-2} + (3 + \tau_s^{-2})\beta_{\text{diff}}]\xi}{\tau_s^{-1}(16/3 + \beta_{\text{diff}})\xi + \tau_s^{-2} + 1}, \quad (42)$$

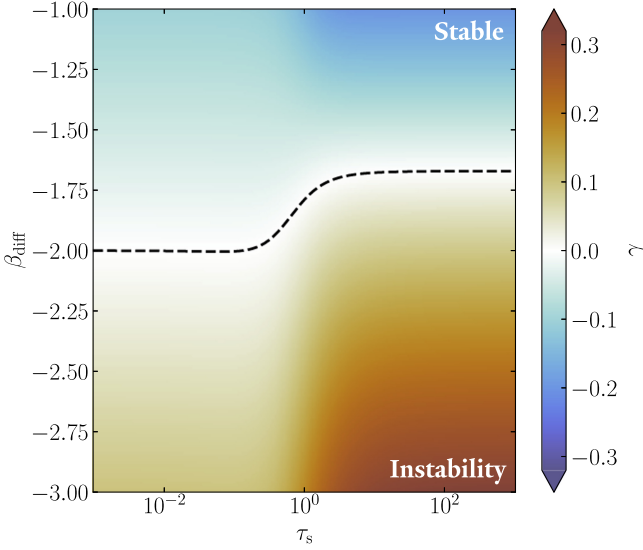


Figure 3. Like Figure 1. Growth rates for the viscous–diffusive instability for $\xi = 0.1$, assuming equal mass and momentum diffusion with $Sc = 1$ and $\beta_{\text{diff}} = \beta_{\text{visc}}$. The black curve corresponds to Equation (40), below which the instability can operate, and above which perturbations are exponentially damped. Note that while parts of the depicted parameter space allow for viscous overstability, this figure only shows the purely real solution. See Section 4.

which in the limits of well-coupled and decoupled particles equals, respectively

$$\gamma \simeq \begin{cases} -\xi(2 + \beta_{\text{diff}}) & \tau_s \ll 1, \\ -\xi(5 + 3\beta_{\text{diff}}) & \tau_s \gg 1. \end{cases} \quad (43)$$

We thus recover Equation (38), in the limit of small stopping times.

Figure 3 shows the real root of the full cubic in Equation (39) for $\xi = 0.1$. The black curve corresponds to Equation (40). For a given β_{diff} , the growth rates are greater for large stopping times. Figure 4 depicts the growth rate of the viscous–diffusive instability for $\beta_{\text{diff}} = \beta_{\text{visc}} = -3$ for various stopping times. Unlike in the inviscid case, where if Equation (36) is satisfied, all modes ξ are unstable (see Figure 2), the viscous–diffusive instability is damped at small scales ($\xi \gtrsim 1$) by viscosity. This regularizes the system, by prohibiting growth on arbitrarily small scales. While our model itself is not applicable to large ξ , one does not expect growth rates to increase without bound at ever-decreasing scales, which is an advantage of including viscosity in the model.

3.3. General Case

Given that numerical constraints on the effective viscosity in the high-density particle midplane of protoplanetary disks are sparse, we finally investigate the most general case our model allows, where we remain agnostic to the value of Sc and retain two independent power-law slopes in δ and α . As before, pure instability is achieved for $A_0 < 0$, which for small ξ results in the condition

$$\frac{1}{\tau_s^2}(2 + \beta_{\text{diff}}) + 3Sc(1 + \beta_{\text{visc}}) < -2. \quad (44)$$

In the general case, the growth rate of the diffusive instability, as well as the existence thereof in the first place, thus depends on five parameters: the stopping time τ_s , Schmidt number Sc ,

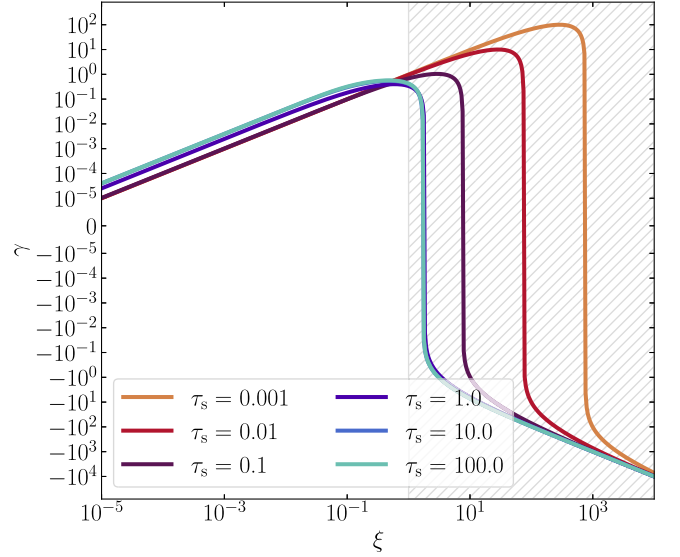


Figure 4. Like Figure 2, but for the viscous–diffusive instability assuming equal mass and momentum diffusion with $Sc = 1$ and $\beta_{\text{diff}} = \beta_{\text{visc}} = -3$, for various stopping times. The viscosity terms damp the instability on small scales, albeit only for $\xi > 1$, where we expect the model to break down. The lines for $\tau_s = 10$ and $\tau_s = 100$ overlap.

diffusion slope β_{diff} , viscosity slope β_{visc} , and dimensionless wavenumber ξ . The Schmidt number Sc acts as an amplification to the viscosity slope in the context of the diffusive instability.

Like in the previous two cases, well-coupled particles with $\tau_s \ll 1$ result in instability if $\beta_{\text{diff}} < -2 - 2\tau_s^2 \approx -2$, on account of the diffusive instability. On the other hand, loosely coupled particles with $\tau_s \gg 1$ are unstable if

$$\beta_{\text{visc}} < -\frac{2}{3}Sc^{-1} - 1. \quad (45)$$

If $Sc \gg 1$, we exactly recover the classical criterion for viscous instability in planetary rings (Ward 1981; Lin & Bodenheimer 1981).

For pure instability with small growth rates, $\gamma \ll 1$, Equation (28) yields $\gamma = -A_0/A_1$, which for $\xi < 1$ results in

$$\gamma = -\frac{\xi[2 + \tau_s^{-2}(2 + \beta_{\text{diff}}) + 3Sc(1 + \beta_{\text{visc}})]}{\tau_s^{-1}(7Sc/3 + 3 + \beta_{\text{diff}})\xi + \tau_s^{-2} + 1}. \quad (46)$$

In the well-coupled limit $\tau_s \ll 1$, this equals the inviscid case in Equation (38). In the loosely coupled limit with $\tau_s \gg 1$, we get

$$\gamma = -\xi[2 + 3Sc(1 + \beta_{\text{visc}})] \quad (\tau_s \gg 1). \quad (47)$$

4. Overstability

We now direct our attention to overstable modes with non-zero ω . Figure 5 shows growth rates of such oscillatory modes as obtained from the full dispersion relation, and demonstrates that large stopping times are required to achieve growing modes. We caution that in this regime, the fluid approximation for the dust grains that underlies our model starts to break down (also see Sections 2.3 and 5.5 as well as Appendix A). We proceed with the analysis for completeness.

For oscillating solutions with $\omega \neq 0$, Equation (32) implies

$$\omega^2 = 3\gamma^2 + 2\gamma A_2 + A_1, \quad (48)$$

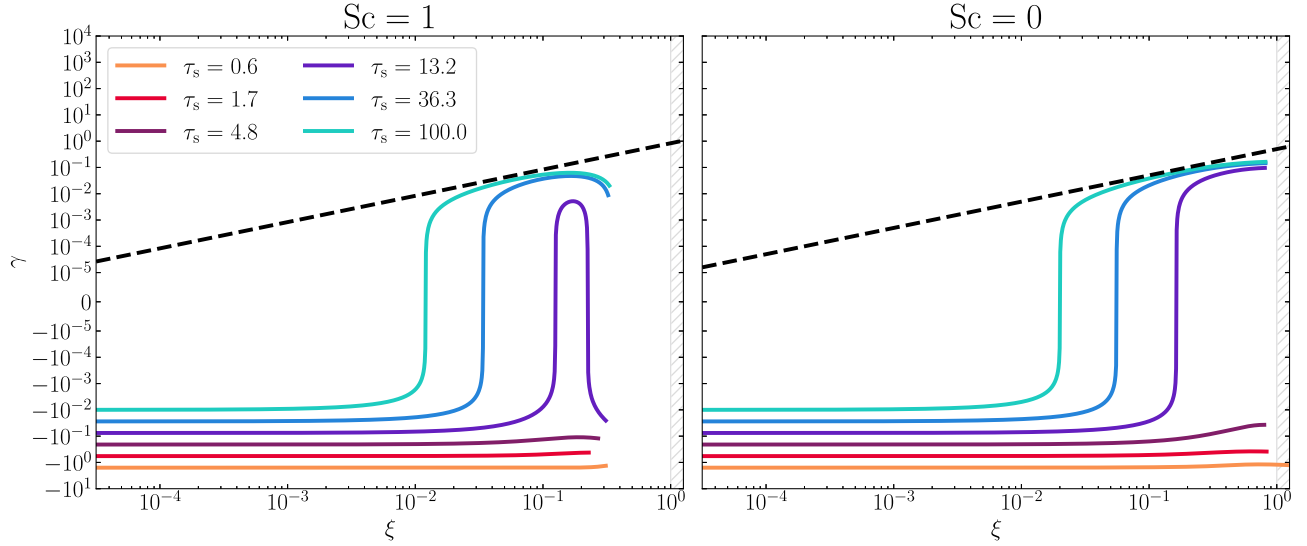


Figure 5. Growth rates for diffusive overstability driven by the viscosity slope ($Sc = 1$, left panel) and driven by the diffusion slope ($Sc = 0$, right panel) for various stopping times obtained from the full dispersion relation in Equation (28). We set $\beta_{\text{visc}} = \beta_{\text{diff}} = 0$ in order to allow for both types of overstability. The dashed lines correspond to Equation (52), which only do not differ substantially between the two panels due to the choice of $\beta_{\text{visc}} = 0$. The lines end once the modes become nonoscillatory (and thus damped), which for large stopping times occur as ξ approaches the hatched region where our model is not applicable.

which is positive definite for $\xi \ll 1$ as seen in Figure 5. When inserted into Equation (33), this results in a cubic for the growth rate of the wave, i.e.,

$$8\gamma^3 + 8A_2\gamma^2 + 2(A_1 + A_2^2)\gamma + A_1A_2 - A_0 = 0. \quad (49)$$

For small growth rates $\gamma \ll 1$, A_1 , and A_2 , the root is

$$\gamma \simeq -\frac{A_1A_2 - A_0}{2(A_1 + A_2^2)}. \quad (50)$$

For $\xi \ll 1$, we have

$$\begin{aligned} \gamma \simeq & -\left\{ \frac{2}{\tau_s^3} + \frac{\xi}{\tau_s^2}(7Sc + 5 + \beta_{\text{diff}}) + \frac{2}{\tau_s} \right. \\ & \left. - \xi \left[1 + 3Sc \left(\frac{2}{9} + \beta_{\text{visc}} \right) \right] \right\} \\ & \times \left(\frac{10}{\tau_s^2} + \frac{\xi}{\tau_s} \left(\frac{70}{3}Sc + 14 + 2\beta_{\text{diff}} \right) + 2 \right)^{-1}. \end{aligned} \quad (51)$$

Assuming large stopping times $\tau_s \gg 1$, this becomes

$$\gamma \sim \frac{\xi}{2} \left[1 + 3Sc \left(\frac{2}{9} + \beta_{\text{visc}} \right) \right], \quad (52)$$

which is plotted in Figure 5 in comparison to the root of the full cubic. For overstability, i.e., growing oscillations, the growth rate must be positive, i.e., $\gamma > 0$, or equivalently

$$\beta_{\text{visc}} \gtrsim -\frac{Sc^{-1}}{3} - \frac{2}{9}, \quad (53)$$

which equals $-5/9$ for $Sc = 1$. Since overstability is characterized by a restoring force which lacks in case of pure instability, this requirement on β_{visc} is opposite in direction compared to the criteria for instability discussed in the previous sections (also compare to the classical viscous overstability, e.g., in Latter & Ogilvie 2006a).

We also note that the $1/Sc$ term in Equation (53) originates from the advection of angular momentum carried by background shear due to the diffusive flux, i.e., the second term on the right-hand side of Equation (13). For $Sc \gg 1$, i.e., negligible diffusion compared to viscosity, this term vanishes and we recover the classical criterion for the viscous overstability in planetary rings (Schmit & Tscharnuter 1995). Interestingly, it is this same term that allows for overstability even in the inviscid case. That is, by setting $Sc = 0$, the growth rate resulting from Equation (51) becomes

$$\gamma = -\frac{2 + \xi\tau_s(5 + \beta_{\text{diff}}) + 2\tau_s^2 - \xi\tau_s^3}{10\tau_s + \xi\tau_s^2(14 + 2\beta_{\text{diff}}) + 2\tau_s^3}, \quad (54)$$

which tends to $\gamma = \xi/2$ for large stopping times $\tau_s \gg 1$ (compare to Equation (52)). Thus, in this limit, the diffusion flux given by the second term on the right-hand side of Equation (13) alone is able to grow epicyclic oscillations.

In Figure 6, we depict growth rates of the diffusive overstability obtained from Equation (51) as a function of the stopping time. The smallest scales have the fastest growth rates and have the least stringent restrictions on the stopping time. For the depicted set of parameters, $\tau_s \gtrsim 10$ leads to overstability on the smallest scales. While this requirement can be further relaxed for larger Sc or more positive β_{visc} , for $\tau_s \lesssim 1$, all oscillating modes are damped.

For this reason, the overstable modes discussed in this section have little physical relevance in the context of particles that generate streaming instability turbulence, where the largest available dust grains are limited at typically $\tau_s \lesssim 1$ (e.g., Birnstiel et al. 2016). We elaborate on this, as well as explore alternative situations where the diffusive overstability may find applicability in Section 5.5.

5. Discussion

In the previous sections, we showed that a dust fluid in protoplanetary disks, which is governed by Equations (1)–(3), can be unstable (Section 3) and overstable (Section 4) when an otherwise constant background state is linearly perturbed,

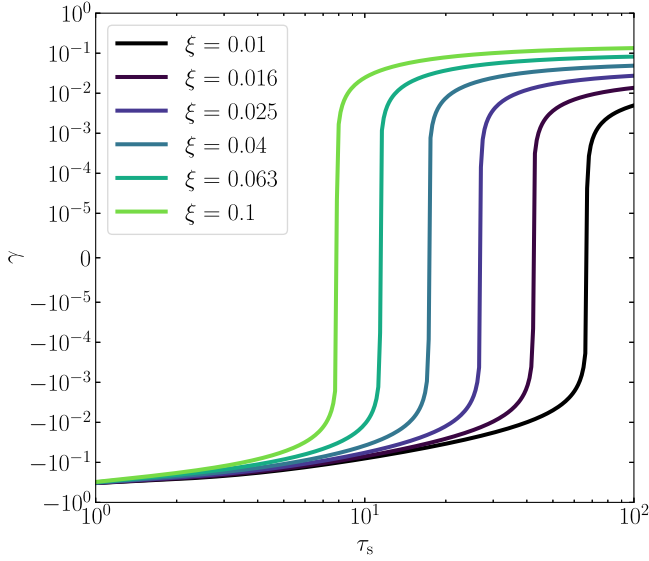


Figure 6. Growth rates for diffusive overstability driven by the viscosity slope ($Sc = 1$) vs. stopping time for various values of ξ , and setting $\beta_{\text{visc}} = \beta_{\text{diff}} = 0$ following Equation (51), which assumes $\xi \ll 1$. For the smallest scales our model applies to, and, given the chosen set of parameters, stopping times of $\tau_s \gtrsim 8$ allow for overstability.

depending on the stopping time of particles and the steepness of the diffusion and viscosity slopes with respect to the dust surface mass density. Here, we discuss and contextualize our findings.

5.1. Physical Picture

First, we reiterate the physical mechanisms that drive the newly found instabilities. Figures 7 and 8 show the growth rates of the full system including both overstability and instability, for the inviscid ($Sc = 0$) and viscous ($Sc = 1$) case, respectively. Guided by the depicted parameter space we can broadly assign the unstable regions into four categories

1. *Diffusive instability driven by the diffusion-dependent pressure.* For small stopping times, the utilized dust pressure prescription (with velocity dispersion $c_d^2 \propto D \propto \Sigma^{\beta_{\text{diff}}}$) can lead to linear instability if the diffusion slope β_{diff} is sufficiently negative (see Equations 36 and 40), and drives particles toward density maxima. The instability is only damped on small scales if the viscosity is nonzero, and has the fastest growth rates on the smallest unstable scales. This instability requires $\tau_s \lesssim 1$, $\beta_{\text{diff}} \lesssim -2$, and if $Sc \gtrsim 1$ also $\xi \lesssim 1$, which for a fiducial $\delta \sim 10^{-5}$ corresponds to wavelengths of $\lambda \gtrsim 0.01H$. The associated growth rates are shown in the top two panels of Figure 7 as well on the left side of the top panel of Figure 8 for small stopping times.
2. *Diffusive instability driven by the viscosity slope.* For nonzero viscosity, the viscosity term dominates over the pressure term for sufficiently large stopping times, leading to a version of the viscous instability (Ward 1981; Lin & Bodenheimer 1981), modified by mass diffusion and the diffusion flux. This instability requires $\tau_s \gtrsim 1$, $Sc \gtrsim 1$, $\xi \lesssim 1$, and $\beta_{\text{visc}} \lesssim -5/3$, and is seen in the top two panels of Figure 8 for large stopping times.
3. *Diffusive overstability driven by the background diffusion flux.* The inclusion of the diffusion flux in Equation (13),

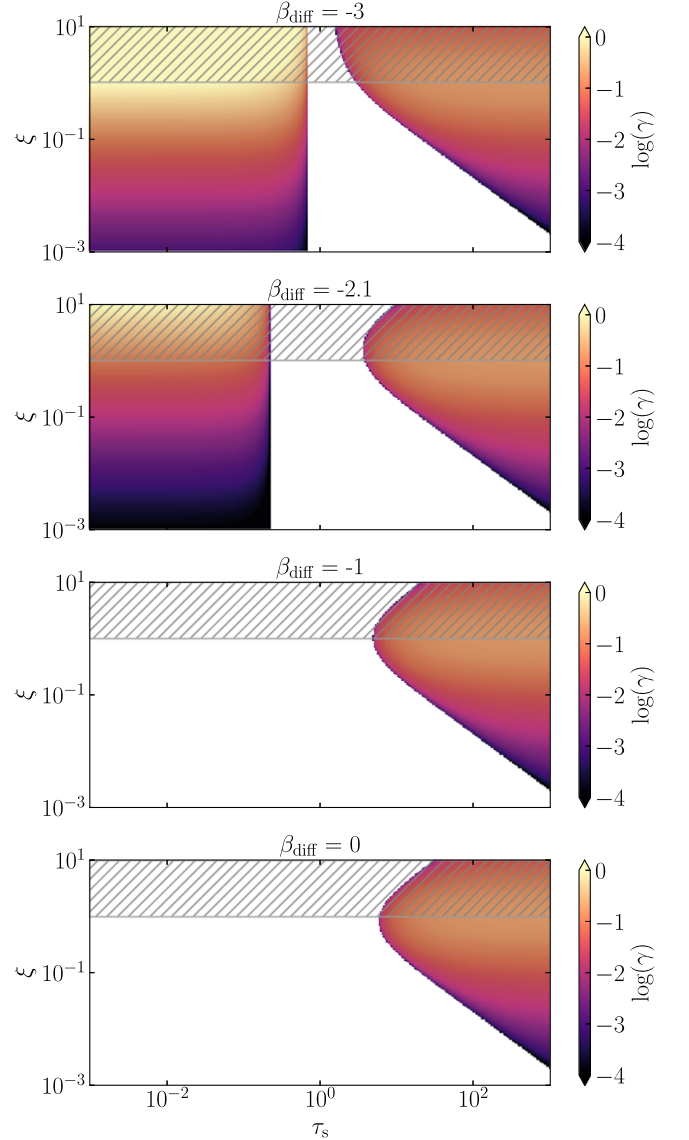


Figure 7. Growth rates for inviscid ($Sc = 0$) diffusive instability and overstability. The diffusion slope β_{diff} increases from top to bottom. The diffusive instability driven by diffusion-dependent pressure is active for all modes ξ if $\beta_{\text{diff}} < -2 - 2\tau_s^2$ (see Equation (36)), which is the case in the upper two panels for small stopping times. For large stopping times, the diffusive overstability driven by the background diffusion flux is active, to first order regardless of the value of β_{diff} .

which radially distributes azimuthal momentum carried by the background shear, provides an additional repellent term that can amplify oscillatory modes if the stopping times are large and viscosity is small. This overstability requires $\tau_s \gtrsim 10$ and $Sc \ll 1$, and is seen in all panels of Figure 7 for large stopping times.

4. *Diffusive overstability driven by the viscosity slope.* Analogously to the classical viscous overstability (Schmit & Tscharnuter 1995), the repellent term that amplifies oscillations is provided by the viscosity slope. This overstability requires $\tau_s \gtrsim 10$, $Sc \gtrsim 1$, $\xi \lesssim 1$, and $\beta_{\text{visc}} \gtrsim -5/9$. The associated growth rates are shown in the bottom panel of Figure 8.

The linear theory describing the diffusive instabilities and overstabilities presented in this work is largely similar to that of

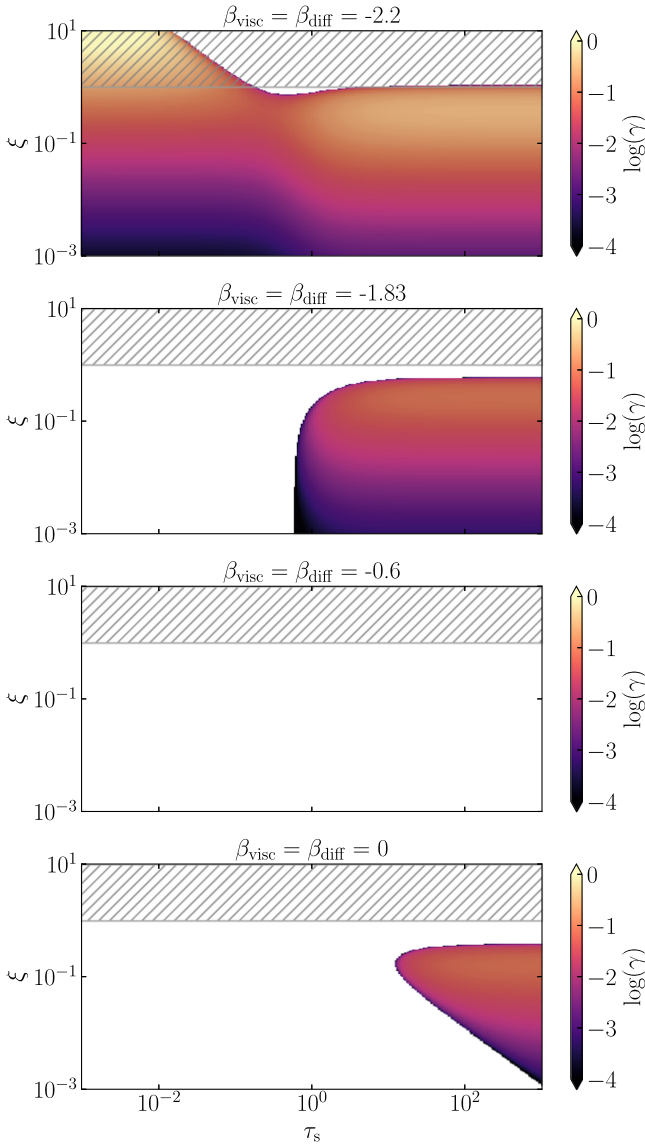


Figure 8. Like Figure 7 but for the viscous–diffusive instability and (modified) viscous overstability with $Sc = 1$. The top panel shows a combination of diffusive instability driven by diffusion-dependent pressure and viscous instability driven by the negative viscosity slope for small and large stopping times (compare to Figure 3). In the panel second from the top, Equation (40) remains satisfied, while Equation (36) is not, so instability is driven by the viscosity slope alone and thus restricted to large τ_s . In the third panel from the top, neither instability is active. When Equation (53) is satisfied (for $Sc = 1$ when β_{visc} exceeds $-5/9$), the (modified) viscous overstability driven by the viscosity slope can be active for large stopping times. Note that for $Sc = 1$, we do not see the purely diffusive overstability as it is damped by viscosity.

the classical viscous instability (Ward 1981; Lin & Bodenheimer 1981) and axisymmetric viscous overstability (Schmit & Tscharnuter 1995) in planetary rings, at least under the neglect of self-gravity and thermal effects, and given the appropriate limits in our model, i.e., $\tau_s \gg 1$ and $Sc \gg 1$. It should be noted though that the physical origin of viscosity and pressure in planetary rings lies in mutual particle collisions, in contrast to the situation depicted in this work, where it results from self-generated turbulence that is external insofar as the model is concerned. Also, a “thin-disk” version of the viscous overstability (i.e., on large radial length scales $\gg H_g$), generated by a constant kinematic shear viscosity, can in principle also

exist in gaseous protoplanetary disks (Latter & Ogilvie 2006a).

In addition, we mention the dust-driven viscous ring instability pioneered by Dullemond & Penzlin (2018) as well as the related instability in Johansen et al. (2011), both of which, although operating on larger scales, are similar in spirit to this paper’s diffusive instabilities. They consider a disk where the gas viscosity is set by turbulence generated from a magneto-rotational instability (Balbus & Hawley 1991), which weakens with increasing dust density through the ionization fraction. It is the viscous gas disk itself that can now be unstable to linear perturbations: an increase in gas density attracts dust grains as they tend to drift toward gas pressure maxima (e.g., Sano et al. 2000); turbulence then weakens and the gas viscosity drops, thereby increasing the gas density further, which attracts more dust, and so on. In our model, we only consider the dust fluid but the decrease in its viscosity, diffusivity, and dust pressure as the dust surface density increases is likewise physically motivated by dust feedback lowering the local diffusive properties of the turbulence generated on small scales.

Indeed, while we motivate our model with streaming instability turbulence and associated measurements of the diffusion slopes (Schreiber & Klahr 2018; Gerbig & Li 2023), it may as well be applicable to other sources of turbulence. For example, the azimuthal streaming instability discovered by Hsu & Lin (2022) has likewise been observed to evolve into filaments once linear modes are saturated. Moreover, if one considers pure gas instabilities as sources of turbulence, the vertical shear instability (Urpin & Brandenburg 1998; Nelson et al. 2013; Lin & Youdin 2015; Barker & Latter 2015; Pfeil & Klahr 2021) or the convective overstability (Klahr & Hubbard 2014; Lyra 2014; Latter 2016) may generate environments suitable for secondary diffusive instabilities. The dependence of the diffusivity and viscosity on the disk parameters would need to be clarified with detailed simulations, but to zeroth order, one expects a drop in turbulence with increasing dust loading, similar to that for the magneto-rotational instability discussed above, because dust feedback tends to stabilize the vertical shear instability (Lin 2019; Lehmann & Lin 2022) and linear convective overstability (Lehmann & Lin 2023).

5.2. Filament Formation through Diffusive Instability

Based on the analytic findings in Sections 3 and 4, we hypothesize that the diffusive instability, driven by a sufficiently negative density dependence of the dust pressure, physically motivated by dust loading reducing diffusivity, may act to amplify density perturbations. These perturbations could then saturate to become marginally stable filaments, as seen in many past simulations (e.g., Johansen & Youdin 2007; Johansen et al. 2009; Carrera et al. 2015; Klahr & Schreiber 2016; Yang et al. 2018; Li et al. 2018; Schreiber & Klahr 2018; Sekiya & Onishi 2018; Gerbig et al. 2020; Flock & Mignone 2021; Li & Youdin 2021; Hsu & Lin 2022; Gerbig & Li 2023).

We visualize the growth of the linear perturbations into such filament-like overdensities in a spacetime diagram of the perturbed density Σ' following Equation (14). Figure 9 shows a perturbation subject to diffusive instability. The chosen set of parameters produces overdensities with a radial spacing of about $0.02H$, which are consistent with the first emergent filaments found in streaming instability simulations (e.g., Li & Youdin 2021).

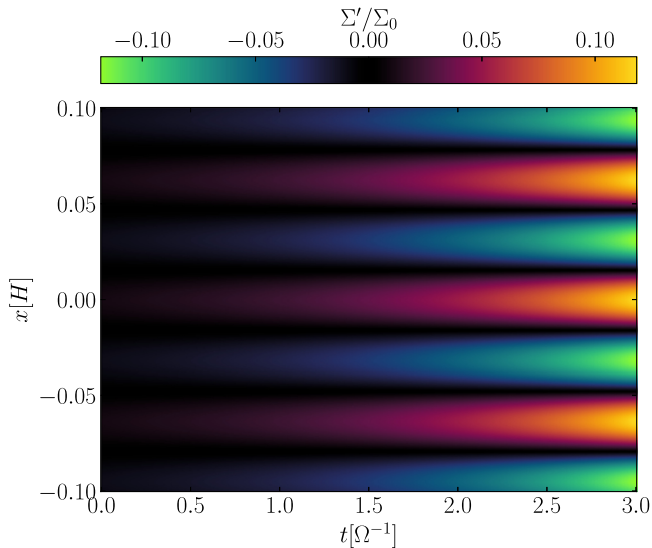


Figure 9. Filament formation shown in a spacetime diagram of a linear perturbation subject to diffusive instability driven by pressure. For this plot, we chose $Sc = 0$, $\tau_s = 0.1$, and $\beta_{\text{diff}} = -3$. We also chose a value of $\delta = 10^{-4}$ and a fast growing mode of $\xi = 0.1$, which corresponds to a physical wavenumber of $k = 100/H$. The eigenvector is scaled with $\hat{\Sigma} = 0.01\Sigma_0$.

Indeed, the diffusive instability has the fastest growth rates on the smallest scale not limited by viscosity ξ_{max} , which is $\xi_{\text{max}} \sim 1$. The corresponding fastest-growing mode is thus expected to be around

$$\frac{\lambda_{\text{fgm}}}{H} = \frac{2\pi}{K} = 2\pi \sqrt{\frac{\delta}{\xi_{\text{max}}}} \approx 2\pi\sqrt{\delta}. \quad (55)$$

For $\delta \sim 10^{-5}$ (e.g., Schreiber & Klahr 2018; Klahr & Schreiber 2020; Gerbig & Li 2023) this would correspond to a consistent value of $\lambda_{\text{fgm}} \sim 0.02H$ (e.g., Li & Youdin 2021). Note that the filament separation in simulations has been found to depend on the external gas pressure slope, stopping time, and dust abundance (e.g., Schreiber & Klahr 2018; Gerbig et al. 2020; Li & Youdin 2021). If these properties influence streaming instability turbulence (e.g., Johansen & Youdin 2007), they are expected to map onto diffusivity and ultimately on the fastest-growing mode in Equation (55). On the other hand, the commonly used fiducial value for the filament feeding zone of $0.2H$ (Yang & Johansen 2014) cannot be directly compared to the scales of interest, as it already involves postformation nonlinear dynamics, such as mergers and breakups.

Figure 10 visualizes the streaming motion that arises from the diffusive instability. Dust is moving toward density maxima, which act as particle traps, in the process amplifying the perturbation.

For comparison, Figure 11 shows traveling waves driven by the diffusive overstability. The shearing sheet is symmetric in x , so waves traveling toward positive x correspond to the complex conjugate of the depicted solution and are equally valid. Note, that the radial bulk velocity is entirely caused by the overstability. If one were to include the background pressure gradient, the flow would pick up a, to first order, constant background drift, which does not affect stability since we can shift into the comoving frame.

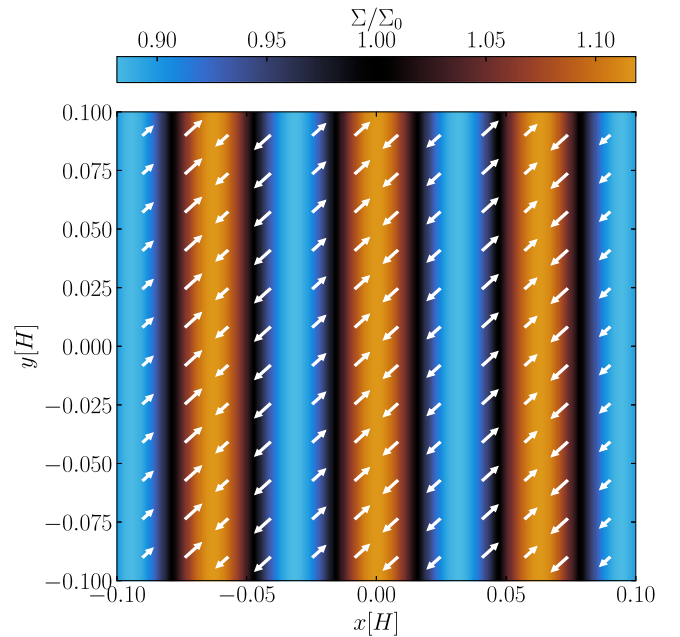


Figure 10. Diffusive instability driven by the diffusion-dependent pressure with the same parameters as in Figure 9. Shown is a map in the x - y space of the particle surface density after a time of $3\Omega^{-1}$, with superimposed rescaled velocity vectors (v'_x, v'_y). The fluid motion is toward density maxima, thus amplifying the perturbation and producing filaments. We show the y -coordinate for better visualization, even though the model itself is axisymmetric.

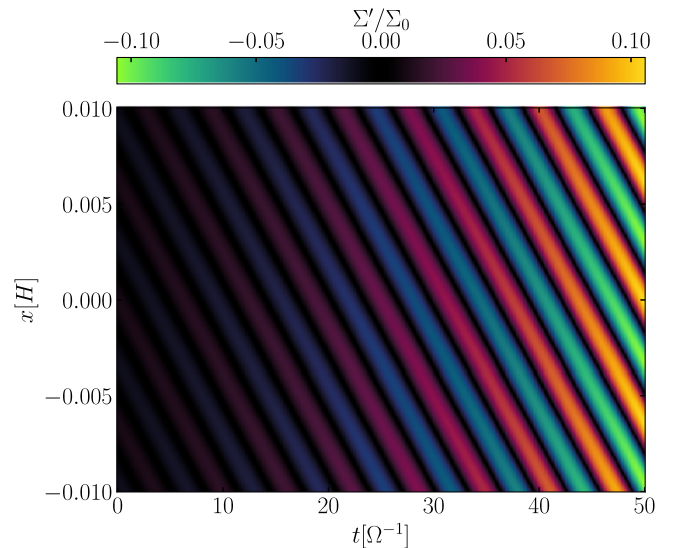


Figure 11. Like Figure 9, but for an oscillatory mode. The linear perturbation is subject to diffusive overstability powered by the background diffusion flux. We chose, $Sc = 0$, $\tau_s = 1000$, $\beta_{\text{diff}} = 0$, and $\hat{\Sigma} = 0.01\Sigma_0$. We took $\delta = 10^{-7}$, at which a mode of $\xi = 0.1$ corresponds to a physical wavenumber of $k = 1000/H$. Note that the shearing sheet is symmetric in x , so waves traveling toward positive x are equally valid.

5.3. Diffusive Instability in the Context of Past Numerical Simulations

The aim of this study is to present a simple linear model for the emergence of the first filaments out of streaming instability turbulence, as seen in a number of simulations including Schreiber & Klahr (2018), Gerbig et al. (2020), Li & Youdin (2021), and Gerbig & Li (2023). Within our model, the required linear growth rates and corresponding required

stopping times that are expected to result in filament formation depend on the values of the diffusion and viscosity slopes β_{diff} and β_{visc} , respectively. Therefore, we aim to contextualize our findings with existing numerical studies and measurements of the aforementioned slopes. As such, our presented theory can most readily be compared to the numerical results presented in Schreiber & Klahr (2018), who performed 2D, nonaxisymmetric, non-self-gravitating shearing sheet simulations of the streaming instability. By conducting a number of simulations at different dust-to-gas ratios and measuring the average particle diffusivity in each simulation, they were able to obtain the slope of diffusion with respect to the dust surface mass density, resulting in values $-2 \lesssim \beta_{\text{diff}} \lesssim -1$, where the exact value depended on the box size and particle stopping time used in their simulations.

While some of the simulations of Schreiber & Klahr (2018) revealed the emergence of filaments with particle concentrations significantly enhanced relative to the ambient background, most did not. In the context of the linear diffusive instability discovered in our work, which requires $\beta_{\text{diff}} \lesssim -2$ (see Figure 3) for instability, the simulations in Schreiber & Klahr (2018) are hence expected to be marginally stable. More recently, Gerbig & Li (2023) measured the diffusion slope within a single vertically stratified shearing box simulation of the streaming instability. They also found $\beta_{\text{diff}} \sim -2$. As this value was obtained *after* the formation of filaments in their simulations, this is also consistent with their simulations being marginally unstable with respect to diffusive instability, provided the saturation of filament growth results in such a marginally stable state.

5.4. Connection to Planetesimal Formation

Within the streaming instability paradigm of planetesimal formation, filaments are often thought to be a necessary precursor for planetesimal formation, as they provide the necessary conditions for subsequent self-gravitational fragmentation. It is therefore of interest to compare the parameter space for active diffusive instability within our model to that determined in numerical simulations of planetesimal formation, specifically clumping thresholds in streaming instability simulations. For this purpose, we can relate metallicity Z to the dust-to-gas ratio $\epsilon = \rho_p/\rho_g$ and diffusivity via (e.g., Lin 2021)

$$Z = \frac{\Sigma}{\Sigma_g} \simeq \epsilon \frac{H_d}{H} \simeq \epsilon \sqrt{\frac{\delta}{\delta + \tau_s}}, \quad (56)$$

where H_d is the vertical scale height of the dust.

Assuming $\tau_s \gg \delta$, we have $\delta \sim \tau_s(Z/\epsilon)^2$. Since our model, and therefore also the diffusive instability mechanism, only implicitly depends on δ via ξ , a change in diffusivity due to a metallicity increase (decrease) can be compensated by a decrease (increase) in wavenumber K toward larger (smaller) radial length scales. For example, the typically fast growing mode of $\xi \sim 1$ corresponds to wavenumbers of $K \sim \epsilon/(Z\sqrt{\tau_s})$.

We proceed by imposing a minimum scale of $\lambda_{\text{crit}} \sim 0.01H$, below which the model does not apply (see Section 2.2), and use this to restrict the maximum allowed ξ , given some value of Z . Specifically, we have

$$\xi_{\text{max}}(Z, \tau_s) = \frac{4\pi^2\delta(Z, \tau_s)}{(\lambda_{\text{crit}}/H)^2} \simeq \left(\frac{2\pi Z/\epsilon}{\lambda_{\text{crit}}/H} \right)^2 \tau_s. \quad (57)$$

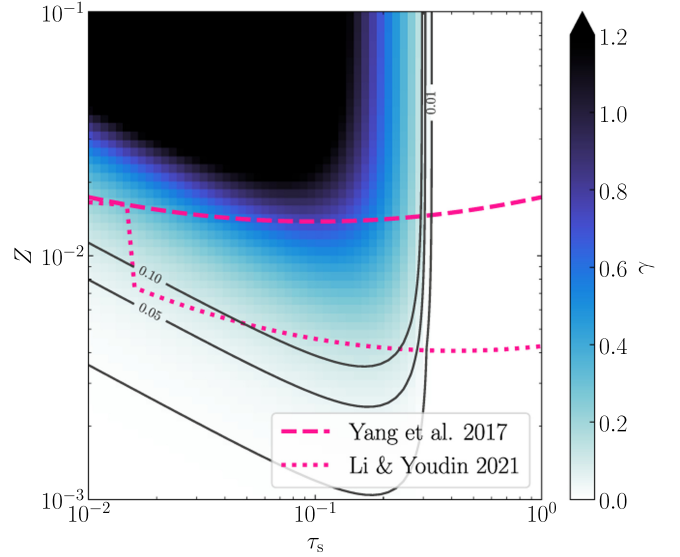


Figure 12. Growth rates of diffusive instability driven by the diffusion-dependent pressure term, depending on the metallicity Z and stopping time τ_s , compared to clumping thresholds in the streaming instability simulations by Yang et al. (2017) and Li & Youdin (2021). We associate a given metallicity Z with the fastest-growing allowed mode ξ of our model via the recipe discussed in Section 5.4 assuming $\epsilon = 1$ and $\lambda_{\text{crit}} = 0.01H$. For the shown growth rates, we also chose $\beta_{\text{diff}} = \beta_{\text{visc}} = -2.2$ and $\text{Sc} = 0$, a favorable set of parameters for diffusive instabilities for small stopping times only.

We then assume that the fastest-growing mode admitted by our model is given by $\xi(Z, \tau_s) = \min(\xi_{\text{fgm}}, \xi_{\text{max}})$, where ξ_{fgm} is the mathematically fastest-growing mode, which is obtained numerically from the full dispersion relation in Equation (28). ξ_{fgm} is typically of order unity (see Figure 2), but may be larger, either in the absence of viscosity or for very small stopping times (see Figures 2 and 4, respectively); or smaller, if the viscosity slope is only marginally more negative than the critically required slope (see the top panel in Figure 8).

Figures 12 and 13 show the growth rates associated with this preferred mode assuming $\epsilon = 1$ and $\lambda_{\text{crit}} = 0.01H$. We also take $\beta_{\text{diff}} = \beta_{\text{visc}} = -2.2$ in both figures. Figure 12 shows the inviscid case with $\text{Sc} = 0$, where only the diffusive instability driven by the diffusion-dependent pressure is possible given the set of parameters, thus suppressing growth for larger stopping times. Overplotted are the clumping thresholds obtained by Yang et al. (2017) and Li & Youdin (2021; also see Carrera et al. 2015 for another version), below which, streaming instability clumping is unlikely to occur. If one takes filament formation due to diffusive instability as a precursor to clumping, then the model depicted in Figure 12 would be inconsistent with the results from the aforementioned simulations, as instability only occurs for stopping times $\tau_s \lesssim 0.3$, in contrast to the results of the simulations.

On the other hand, Figure 13 shows growth rates associated with the same set of parameters, except that now $\text{Sc} = 1$. Now, in principle, particles with any value $\tau_s \lesssim 1$ can be unstable to diffusive instability driven by the viscosity slope, which produces similar growth rates. Thus, in this model, the entire parameter space, probed by the studies Yang et al. (2017) and Li & Youdin (2021), is subject to diffusive instabilities, rendering the model consistent with the hypothesis that planetesimal formation is triggered by the emergence of filaments induced by diffusive instability.

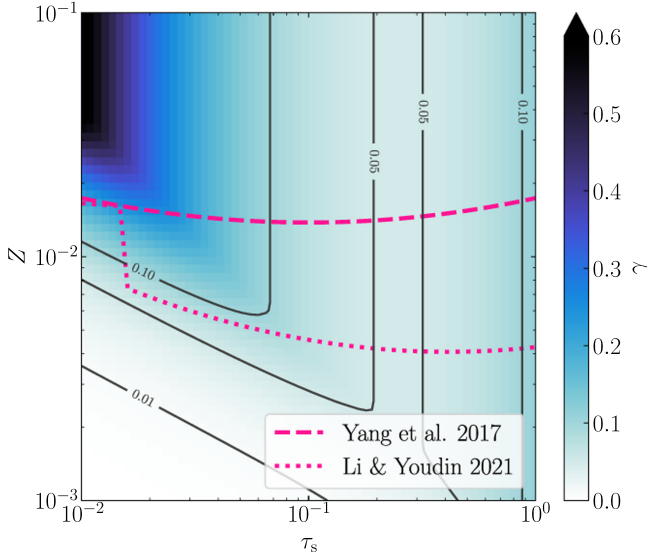


Figure 13. Like Figure 12 but now for $Sc = 1$, which allows for instability driven by the viscosity slope at large stopping times in addition to the instability driven by the diffusion-dependent pressure term. The other parameter choices are identical to those in Figure 12.

We note that the models displayed in Figures 12 and 13 contain a number of parameters (λ_{crit} , ϵ , β_{diff} , β_{visc} , and Sc) which we chose relatively freely and assumed to be independent of τ_s in order to get a prototype idea if there may be a connection to planetesimal formation. The resulting first estimations insinuate that a model which includes viscosity in addition to mass diffusion is more able to explain the threshold for planetesimal formation as determined in simulations, as only then, diffusive instability can also operate for stopping times of $\tau_s \gtrsim 0.3$, in agreement with planetesimal formation in simulations. More detailed calculations, in concert with additional numerical constraints on diffusion and viscosity slopes, are required to assess further the diffusion instability’s role in planetesimal formation.

5.5. Instability and Overstability at Large Stopping Times?

The local axisymmetric viscous overstability of a thin astrophysical disk has extensively been studied in the context of Saturn’s dense rings, employing hydrodynamic models (Schmit & Tscharnuter 1995, 1999; Spahn et al. 2000; Schmidt et al. 2001; Schmidt & Salo 2003; Latter & Ogilvie 2009, 2010; Lehmann et al. 2017, 2019), kinetic models (Latter & Ogilvie 2006b, 2008), and N -body simulations (Salo et al. 2001; Rein & Latter 2013; Ballouz et al. 2017; Lehmann et al. 2017; Mondino-Llermanos & Salo 2023). Based on the results from the hydrodynamic and N -body simulations, overstability in Saturn’s rings typically saturates in the form of nonlinear traveling wave trains that could in principle carry appreciable amounts of angular momentum. Wave trains are often interspersed by defect structures, which may act as sources or sinks of the former. Indeed, viscous overstability is the most promising mechanism to explain the occurrence of periodic fine structures on a ~ 100 m scale in parts of Saturn’s A and B rings, which have directly been observed (Thomson et al. 2007; Colwell et al. 2007; Hedman et al. 2014). It is thus of interest to explore the conditions under which we expect the diffusive overstability to operate in overdense particle layers in protoplanetary disks.

Since this requires $\tau_s \gtrsim 1$, we preface further discussion by reiterating that the hydrodynamical model is strictly not applicable for large stopping times, and instead a kinetic model should be used (see Section 2.3).

As outlined in Section 5.1, in addition to the diffusive instability driven by the pressure term, there are three types of instabilities that can arise for large stopping times. While instability and overstability driven by the viscosity slope have specific requirements on β_{visc} , diffusive overstability can operate if $Sc \ll 1$ regardless of the value of the diffusion slope β_{diff} (see Figure 7).

The questions are (a) to what extent the inviscid, hydrodynamic model can still appropriately describe the system for $\tau_s \gtrsim 1$, whether or not particles with sufficiently large stopping times (b) can exist, and (c) is their turbulent behavior still well characterized by the diffusive flux model that shapes the continuity equation, the pressure model, and the angular momentum conserving terms in the momentum equations.

Indeed, in the classical picture of particle growth in protoplanetary disks, stopping times are limited at around $\tau_s \sim 1$ (e.g., Birnstiel et al. 2012, 2016), and as such, individual particles that qualify for diffusive overstability would already be considered planetesimal-sized objects. Another possible pathway of getting objects with large stopping times was suggested by Johansen & Youdin (2007). In an effort to explain unexpected drift rates of particle clumps found in their streaming instability simulations, they hypothesize that a clump may collectively have an increased stopping time relative to the individual grains, due to shielding each other from the gas stream and providing an order-of-magnitude scaling

$$\tau_s^{\text{eff}} \sim \epsilon \frac{R_{\text{clump}}}{\eta r} \frac{\eta r \Omega}{\Delta v}, \quad (58)$$

with R_{clump} being the clump’s radius and Δv its velocity relative to the gas. While such clumps are far too few in number density to be appropriately modeled by a fluid approach, we adapt this hypothesized collective shielding effect to our situation.

Specifically, applying Johansen & Youdin (2007)’s argument to the quasisteady, turbulent dust layer that we envision as being in equilibrium, we set $R_{\text{clump}} = H_d$ as the dust scale height. Then, using $H_d = ZH/\epsilon$ from Equation (56), we find $\tau_s^{\text{eff}} \sim Z/\Pi$, where $\Pi \equiv \eta/(Hr)$ is the reduced radial pressure gradient parameter, again taking $\Delta v \sim \eta r \Omega$. The diffusive overstability’s requirements of $\tau_s^{\text{eff}} \gtrsim 1$ translates to $Z \gtrsim \Pi$, and the same applies for the diffusive instability driven by the viscosity slope. Coincidentally, Bai & Stone (2010) find that clumping via the streaming instability becomes easier with smaller Π . Similarly, at fixed τ_s (the stopping time for individual grains), Sekiya & Onishi (2018) find filament formation in their streaming instability simulations if $\sqrt{2\pi} Z/\Pi \gtrsim 1$. We can interpret these results within our model as filaments only form if the effective stopping time, realized through Z/Π , exceeds unity in order to trigger the diffusive overstability (or the diffusive instability driven by the viscosity slope).

The streaming instability formally still operates for $\tau_s \gtrsim 1$ as the growth rates only decrease slowly with stopping time (Pan 2020). However, due to the lack of numerical constraints on the diffusivity in this regime, it is unclear to what extent instabilities and overstabilities would develop on the scales within our model’s validity, even if the diffusion and viscosity slopes were to remain unchanged. Since, in order to achieve instability on

the relevant scales, the diffusivities cannot be arbitrarily small, we consider the possibility of diffusion to not be self-generated. Instead, diffusion may stem directly from a turbulent gas, the diffusivity and viscosity of which we denote as δ_g and α_g , respectively.

In the preceding sections, we were exclusively concerned with particle diffusivity δ , which we treated as wholly independent from τ_s . While this is mathematically self-consistent, it does not necessarily reflect physical conditions. Indeed, an increased particle response time to turbulence diminishes the diffusion experienced by the particles as (Youdin 2011)

$$\delta = \frac{1 + \tau_s + 4\tau_s^2}{(1 + \tau_s^2)^2} \delta_g, \quad (59)$$

which reduces to $\delta \sim \delta_g$ for small stopping times, but becomes $\delta \sim \delta_g/\tau_s^2$ for large stopping times. That is, large grains feel a much reduced turbulence than that in the gas.

Consider, for example, gas with a fiducial diffusivity of $\delta_g \sim \alpha_g \sim 10^{-3}$, which is a typical value in numerical simulations of vertical shear instability or magneto-rotational instability (e.g., Flock et al. 2017). For $\tau_s \sim 10$, this would lead to $\delta \sim 10^{-5}$, which is comparable to the diffusivities generated by streaming instability with smaller particles. The fastest-growing scale per Equation (55) remains unchanged at $\sim 0.02H$. Indeed, since the diffusive instabilities discussed in this paper depend on $\xi = \delta K^2$ only, any decrease in the diffusivity due to particle response to turbulence would only shift the fastest-growing mode down to smaller scales, but not prohibit the mechanism itself from operating.

We thus argue that the large stopping time instability and overstabilities may find applicability if a big enough collection of large stopping time particles are available in protoplanetary disks, or if the dust layer has a collective stopping time that exceeds unity. Note, that this estimation ignored the effect of the particle layer on gas turbulence, i.e., δ_g itself. For example, turbulence driven by the vertical shear instability is damped by dust feedback, even when the dust-to-gas ratio is less than unity (e.g., Lin 2019).

5.6. Caveats and Additional Considerations

Our vertically averaged model neglects vertical motions. Therefore, inertial waves are discarded, such that the classical, axisymmetric streaming instability is not captured by our model (Squire & Hopkins 2018), even if we were to include the gas equations with a radial background pressure gradient. While we attribute the underlying turbulence, characterized by diffusion and viscosity of the dust fluid, to the streaming instability (or an equivalent mechanism), filament formation in our model is not a direct result of this underlying, small-scale instability. Instead, it originates from one or more intrinsic large-scale instabilities of the midplane dust layer, described by our model. In order to neglect gas perturbations, our model is time averaged over one turbulent correlation time. As a result, linear modes with frequencies smaller than one inverse correlation time should be considered with caution. Future work should include the dynamical equations describing the gas, as well as the vertical dimension, to investigate filament formation via streaming-type instabilities with variable viscosity and diffusivity in a more rigorous manner.

In our model, the diffusion and viscosity slope is assumed to depend on the dust surface density only, primarily because of

the available numerical constraints from Schreiber & Klahr (2018) and Gerbig & Li (2023) and due to the analogy to isothermal hydrodynamic models for viscous instabilities in planetary rings. However, if diffusion and viscosity indeed arise from small-scale streaming instabilities, other dependencies are conceivable, namely a relative dust–gas streaming velocity which powers the streaming instability in the first place.

We also neglect particle self-gravity as filaments already form before self-gravity is turned on in simulations (e.g., Schreiber & Klahr 2018; Gerbig et al. 2020; Gerbig & Li 2023). Nonetheless, self-gravity may have importance, modifying the instability criteria and growth rates. To first order, it has a destabilizing effect and would amplify density enhancements, as well as permit gravitational instabilities (e.g., Youdin & Shu 2002; Youdin 2011; Tominaga et al. 2019, 2023; Gerbig et al. 2020; Gerbig & Li 2023). We reserve this topic for subsequent studies.

Lastly, we also ignored the possibility of a polydispersed dust fluid with a distribution of stopping times, and instead asserted a single stopping time, which is reasonable for a top-heavy size distribution (e.g., Birnstiel et al. 2012). Still, the damping effect of particle size distributions on the streaming instability (Krapp et al. 2019; Paardekooper et al. 2020; Zhu & Yang 2021; Yang & Zhu 2021) underscores that this is a relevant point to keep in mind in future investigations of diffusive instabilities.

6. Summary

In this work we present a novel, vertically averaged axisymmetric hydrodynamic model for a dense particle layer embedded in a gaseous protoplanetary disk. The dust being dominant, we model the effect of gas as a perturbation on the dust dynamics by evoking drag forces, mass diffusion, viscosity, and pressure of the dust. The pressure is assumed to depend on the dust diffusivity following a sedimentation–diffusion ansatz, and diffusivity and viscosity are allowed to depend on the dust surface mass density. We find that our model supports a variety of linear diffusion and oscillatory instabilities.

The diffusion instabilities arise if the dust particles’ diffusion and/or viscosity decrease sufficiently fast with increasing particle surface mass density, which is motivated by the results of past simulations. Specifically, for well-coupled particles with $\tau_s \ll 1$, the diffusion-dependent pressure can destabilize the particle flow if the mass diffusion slope with respect to the dust surface mass density is sufficiently negative. On the other hand, for decoupled particles $\tau_s \gtrsim 1$, instability is driven by the viscosity slope, similar to the viscous instability in planetary rings.

The main application of our model is a dense midplane particle layer subject to turbulence generated by the streaming instability on small scales. Indeed, the diffusivities associated with streaming instability turbulence measured in past simulations are found to be sufficient for the diffusive instabilities in our model to possess appreciable growth rates on the order of the dynamical timescale, and radial length scales that are characteristic of overdense particle filaments seen in numerical simulations of the streaming instability. Based on these findings we argue that diffusive instabilities as captured by our model may play a role in filament formation within dusty

protoplanetary disks, which is a key step within the streaming instability paradigm of planetesimal formation.

In addition, our model can also give rise to growing oscillatory modes. In the inviscid case, large stopping times τ_s can in principle result in overstable modes on a wide range of radial length scales, regardless of the diffusion slope, as the radial diffusion flux alone can provide the necessary repellent acceleration. In the presence of viscosity, this overstability is damped, unless the viscosity slope is sufficiently flat. In this case, the overstability behaves similar to the axisymmetric viscous overstability in planetary rings. Whether or not this instability has applicability in protoplanetary disks is unclear, as it relies strongly on the particles possessing large stopping times $\tau_s > 1$, as well as their interaction with the gas turbulence.

More detailed analytical investigations including vertical motions and an explicit inclusion of gas within a two-fluid formalism, accompanied by additional numerical constraints on diffusivity, viscosity, as well as their slopes, will be crucial to pinpoint further the relevance of diffusive instabilities in dusty protoplanetary disks, filament formation therein, and planetesimal formation.

Acknowledgments

We are appreciative to the reviewer, whose discerning feedback was invaluable in refining the paper. K.G. thanks Rixin Li, Ryosuke Tominaga, Tiger Lu, and Greg Laughlin for efficacious discussions. This work is supported by the National Science and Technology Council through grants 112-2112-M-001-064 and 112-2124-M-002-003 and through an Academia Sinica Career Development Award (AS-CDA-110-M06). K.G. acknowledges generous support from the Heising-Simons Foundation through Grant 2021-2802 to Yale University.

Software: NumPy (Harris et al. 2020), Matplotlib (Hunter 2007), and CMasher (van der Velden 2020).

Appendix A

Justification for Chosen Hydrodynamic Equations

We utilize Reynolds averaging to justify the basic equations used in our model. Hereby, we decompose the instantaneous physical variable A into average $\langle A \rangle$ and short-term ΔA fluctuations with the property $\langle \Delta A \rangle = 0$.

Consider the continuity equation for surface density

$$\frac{\partial \Sigma}{\partial t} + \frac{1}{r} \frac{\partial (r \Sigma v_r)}{\partial r} = 0, \quad (\text{A1})$$

and the radial and azimuthal momentum equations

$$\frac{\partial (\Sigma v_r)}{\partial t} + \frac{1}{r} \frac{\partial}{\partial r} (r \Sigma v_r^2) = \Sigma \frac{v_\phi^2}{r} + \Sigma \Omega^2 r - \Sigma \frac{v_r - u_r}{t_s}, \quad (\text{A2})$$

$$\frac{\partial (\Sigma v_\phi)}{\partial t} + \frac{1}{r} \frac{\partial}{\partial r} (r \Sigma v_\phi v_r) = -\Sigma \frac{v_\phi v_r}{r} - \Sigma \frac{v_\phi - u_\phi}{t_s}, \quad (\text{A3})$$

respectively, for an axisymmetric dust disk. The left-hand side of both momentum equations is the rate of change of the momentum expressed as the sum of the Eulerian derivative and advection term. The right-hand side of Equation (A2) includes a curvature term, external gravitational potential, and a drag term. The right-hand side of Equation (A3) includes a curvature term and drag term only. Reynolds decomposition and

subsequent averaging yields (compare to, e.g., Cuzzi et al. 1993; Tominaga et al. 2019)

$$\frac{\partial \langle \Sigma \rangle}{\partial t} + \frac{1}{r} \frac{\partial (r \langle \Sigma \rangle \langle v_r \rangle)}{\partial r} = -\frac{1}{r} \frac{\partial}{\partial r} r \langle \Delta \Sigma \Delta v_r \rangle, \quad (\text{A4})$$

$$\begin{aligned} & \langle \Sigma \rangle \frac{\partial \langle v_r \rangle}{\partial t} + \frac{\partial}{\partial t} \langle \Delta \Sigma \Delta v_r \rangle + \langle \Sigma \rangle \langle v_r \rangle \frac{\partial \langle v_r \rangle}{\partial r} \\ &= \langle \Sigma \rangle \frac{\langle v_\phi \rangle^2}{r} + \langle \Sigma \rangle \Omega^2 r - \langle \Sigma \rangle \frac{\langle v_r \rangle - \langle u_r \rangle}{t_s} \\ & \quad - \frac{\langle \Delta \Sigma (\Delta v_r - \Delta u_r) \rangle}{t_s} + \frac{1}{r} \frac{\partial (r \sigma_{rr})}{\partial r} - \frac{\sigma_{\phi\phi}}{r} \\ & \quad + \frac{2 \langle \Delta \Sigma \Delta v_\phi \rangle \langle v_\phi \rangle}{r} - 2 \langle \Delta \Sigma \Delta v_r \rangle \frac{\partial \langle v_r \rangle}{\partial r} \\ & \quad - \langle v_r \rangle \frac{1}{r} \frac{\partial}{\partial r} (r \langle \Delta \Sigma \Delta v_r \rangle), \end{aligned} \quad (\text{A5})$$

$$\begin{aligned} & \langle \Sigma \rangle \frac{\partial \langle v_\phi \rangle}{\partial t} + \frac{\partial}{\partial t} \langle \Delta \Sigma \Delta v_\phi \rangle + \langle \Sigma \rangle \langle v_r \rangle \frac{\partial \langle v_\phi \rangle}{\partial r} \\ &= -\langle \Sigma \rangle \frac{\langle v_r \rangle \langle v_\phi \rangle}{r} - \langle \Sigma \rangle \frac{\langle v_\phi \rangle - \langle u_\phi \rangle}{t_s} - \frac{\langle \Delta \Sigma (\Delta v_\phi - \Delta u_\phi) \rangle}{t_s} \\ & \quad - \langle \Delta \Sigma \Delta v_r \rangle \frac{\langle v_\phi \rangle}{r} - \frac{1}{r} \frac{\partial}{\partial r} (r \langle \Delta \Sigma \Delta v_\phi \rangle \langle v_r \rangle) \\ & \quad - \langle \Delta \Sigma \Delta v_r \rangle \frac{\partial \langle v_\phi \rangle}{\partial r} - \langle \Delta \Sigma \Delta v_\phi \rangle \frac{\langle v_r \rangle}{r} \\ & \quad + \frac{1}{r} \frac{\partial}{\partial r} (r \sigma_{r\phi}) + \frac{\sigma_{r\phi}}{r}, \end{aligned} \quad (\text{A6})$$

where we introduced the components of the Reynolds stress tensor as

$$\sigma_{rr} = -\langle \Sigma \rangle \langle \Delta v_r^2 \rangle - \langle \Delta \Sigma \Delta v_r^2 \rangle, \quad (\text{A7})$$

$$\sigma_{\phi\phi} = -\langle \Sigma \rangle \langle \Delta v_\phi^2 \rangle - \langle \Delta \Sigma \Delta v_\phi^2 \rangle, \quad (\text{A8})$$

$$\sigma_{r\phi} = -\langle \Sigma \rangle \langle \Delta v_r \Delta v_\phi \rangle - \langle \Delta \Sigma \Delta v_r \Delta v_\phi \rangle. \quad (\text{A9})$$

Following Cuzzi et al. (1993) and Tominaga et al. (2019), we ignore the second terms on the left-hand side of both momentum equations. We also assume that the terms $t_s^{-1} \langle \Delta \Sigma (\Delta v_r - \Delta u_r) \rangle$ and $t_s^{-1} \langle \Delta \Sigma (\Delta v_\phi - \Delta u_\phi) \rangle$ vanish, which is the case if $\Delta v_r = \Delta u_r$ and $\Delta v_\phi = \Delta u_\phi$, as assumed in Cuzzi et al. (1993) and Tominaga et al. (2019).

Next, we assert the following set of closure relations

$$\langle \Delta \Sigma \Delta v_r \rangle = -D \frac{\partial \langle \Sigma \rangle}{\partial r}, \quad (\text{A10})$$

$$\langle \Delta \Sigma \Delta v_\phi \rangle = -\frac{D}{r} \frac{\partial \langle \Sigma \rangle}{\partial \phi} = 0, \quad (\text{A11})$$

$$\langle \Delta \Sigma \Delta v_r^2 \rangle = \langle \Delta \Sigma \Delta v_\phi^2 \rangle = -T_{rr} = -T_{\phi\phi}, \quad (\text{A12})$$

$$\langle \Sigma \rangle \langle \Delta v_r \Delta v_\phi \rangle + \langle \Delta \Sigma \Delta v_r \Delta v_\phi \rangle = -T_{r\phi} = -T_{\phi r}, \quad (\text{A13})$$

$$\langle \Delta v_r^2 \rangle = \langle \Delta v_\phi^2 \rangle = c_d^2. \quad (\text{A14})$$

Equations (A10) and (A11) are the gradient diffusion hypothesis (see Cuzzi et al. 1993; Goodman & Pindor 2000; Schräpler & Henning 2004; Shariff & Cuzzi 2011; Huang & Bai 2022; Binkert 2023). Equation (A14) defines the effective particle velocity dispersion (Cuzzi et al. 1993; Tominaga et al. 2019). Finally, Equations (A12) and (A13) employ the Boussinesq

hypothesis (also see Binkert 2023) for the dust fluid and in the process introduce viscosity into the problem via the viscous stress tensor in Equation (6)—a choice that relates it to the Reynolds stress tensor components via

$$\sigma_{rr} = -\langle \Sigma \rangle c_d^2 + T_{rr} = \sigma_{\phi\phi} = -\langle \Sigma \rangle c_d^2 + T_{\phi\phi}, \quad (\text{A15})$$

$$\sigma_{r\phi} = T_{r\phi} = \sigma_{\phi r} = T_{\phi r}. \quad (\text{A16})$$

The correlations in Equations (A12) and (A13) are dropped in Tominaga et al. (2019). For $\nu = 0$, our closure relations are thus identical to theirs. Huang & Bai (2022) additionally drop the pressure term in Equation (A14).

The closure relations in Equations (A10)–(A14) establish a Newtonian stress–strain relation for the particle fluid, in the process removing the need for an evolution equation for the stress tensor. This becomes questionable for $\tau_s > 1$, where a kinetic approach is preferred over this fluid dynamical treatment (see Jacquet et al. 2011; Section 2.3).

Using the gradient diffusion hypothesis, the continuity equation can directly be rewritten as an advection–diffusion equation, i.e.,

$$\frac{\partial \langle \Sigma \rangle}{\partial t} + \frac{1}{r} \frac{\partial (r \langle \Sigma \rangle \langle v_r \rangle)}{\partial r} = \frac{1}{r} \frac{\partial}{\partial r} \left(r D \frac{\partial \langle \Sigma \rangle}{\partial r} \right). \quad (\text{A17})$$

In the momentum equations, all terms containing $\langle \Delta \Sigma \Delta v_\phi \rangle$ drop due to axisymmetry. We are left with

$$\begin{aligned} \langle \Sigma \rangle \frac{\partial \langle v_r \rangle}{\partial t} + \langle \Sigma \rangle \langle v_r \rangle \frac{\partial \langle v_r \rangle}{\partial r} &= \langle \Sigma \rangle \frac{\langle v_\phi \rangle^2}{r} + \langle \Sigma \rangle \Omega^2 r \\ &- \langle \Sigma \rangle \frac{\langle v_r \rangle - \langle u_r \rangle}{t_s} - \frac{\partial (c_d^2 \langle \Sigma \rangle)}{\partial r} + \langle \Sigma \rangle \tilde{F}_r, \end{aligned} \quad (\text{A18})$$

$$\begin{aligned} \langle \Sigma \rangle \frac{\partial \langle v_\phi \rangle}{\partial t} + \langle \Sigma \rangle \langle v_r \rangle \frac{\partial \langle v_\phi \rangle}{\partial r} &= -\langle \Sigma \rangle \frac{\langle v_r \rangle \langle v_\phi \rangle}{r} \\ &- \langle \Sigma \rangle \frac{\langle v_\phi \rangle - \langle u_\phi \rangle}{t_s} + \langle \Sigma \rangle \tilde{F}_\phi, \end{aligned} \quad (\text{A19})$$

where we defined

$$\begin{aligned} \langle \Sigma \rangle \tilde{F}_r &= \frac{1}{r} \frac{\partial}{\partial r} (r T_{rr}) - \frac{T_{\phi\phi}}{r} + \frac{1}{r} \frac{\partial}{\partial r} \left(r D \langle v_r \rangle \frac{\partial \langle \Sigma \rangle}{\partial r} \right) \\ &+ D \frac{\partial \langle \Sigma \rangle}{\partial r} \frac{\partial \langle v_r \rangle}{\partial r}. \end{aligned} \quad (\text{A20})$$

$$\begin{aligned} \langle \Sigma \rangle \tilde{F}_\phi &= \frac{1}{r} \frac{\partial}{\partial r} (r T_{r\phi}) + \frac{T_{r\phi}}{r} + \frac{\langle v_\phi \rangle}{r} D \frac{\partial \langle \Sigma \rangle}{\partial r} \\ &+ D \frac{\partial \langle \Sigma \rangle}{\partial r} \frac{\partial \langle v_\phi \rangle}{\partial r}. \end{aligned} \quad (\text{A21})$$

The first two terms in both equations are just the radial and azimuthal components of the divergence (in cylindrical coordinates) of the viscous stress tensor, respectively, i.e.,

$$F_r = \frac{1}{\langle \Sigma \rangle} (\nabla \cdot T_{ij})_r = \frac{1}{\langle \Sigma \rangle} \left(\frac{1}{r} \frac{\partial}{\partial r} (r T_{rr}) - \frac{T_{\phi\phi}}{r} \right), \quad (\text{A22})$$

$$F_\phi = \frac{1}{\langle \Sigma \rangle} (\nabla \cdot T_{ij})_\phi = \frac{1}{\langle \Sigma \rangle} \left(\frac{1}{r} \frac{\partial}{\partial r} (r \sigma_{r\phi}) + \frac{\sigma_{r\phi}}{r} \right). \quad (\text{A23})$$

The remaining terms in $\langle \Sigma \rangle \tilde{F}_r$ and $\langle \Sigma \rangle \tilde{F}_\phi$ were already derived by Tominaga et al. (2019) and are associated with the bulk transport of momentum by the diffusion flux as well as the

diffusive transport of bulk momentum. We thus can rewrite the momentum equations into the form

$$\begin{aligned} \langle \Sigma \rangle \frac{\partial \langle v_r \rangle}{\partial t} + \left(\langle \Sigma \rangle \langle v_r \rangle - D \frac{\partial \langle \Sigma \rangle}{\partial r} \right) \frac{\partial \langle v_r \rangle}{\partial r} \\ = \langle \Sigma \rangle \frac{\langle v_\phi \rangle^2}{r} + \langle \Sigma \rangle \Omega^2 r - \langle \Sigma \rangle \frac{\langle v_r \rangle - \langle u_r \rangle}{t_s} - \frac{\partial (c_d^2 \langle \Sigma \rangle)}{\partial r} \\ + \frac{1}{r} \frac{\partial}{\partial r} \left(r D \langle v_r \rangle \frac{\partial \langle \Sigma \rangle}{\partial r} \right) + \langle \Sigma \rangle F_r, \end{aligned} \quad (\text{A24})$$

$$\begin{aligned} \langle \Sigma \rangle \frac{\partial \langle v_\phi \rangle}{\partial t} + \left(\langle \Sigma \rangle \langle v_r \rangle - D \frac{\partial \langle \Sigma \rangle}{\partial r} \right) \frac{\partial \langle v_\phi \rangle}{\partial r} \\ = -\frac{\langle v_\phi \rangle}{r} \left(\langle \Sigma \rangle \langle v_r \rangle - D \frac{\partial \langle \Sigma \rangle}{\partial r} \right) \\ - \langle \Sigma \rangle \frac{\langle v_\phi \rangle - \langle u_\phi \rangle}{t_s} + \langle \Sigma \rangle F_\phi. \end{aligned} \quad (\text{A25})$$

Dividing by $\langle \Sigma \rangle$ leads to Equations (2) and (3). For clarity we omit the brackets $\langle \rangle$ in the paper’s main text. Note, that unlike Klahr & Schreiber (2021), we specifically keep the drag term in the azimuthal momentum equation.

Appendix B Dust Pressure Model

Appendix A uses Reynolds averaging to derive a pressure-like force term of the form $\partial P / \partial r$ in the radial momentum equation, where $P = c_d^2 \Sigma$ can be understood as the effective dust pressure, with velocity dispersion c_d , which we allow to vary with density.

Specifically, following Klahr & Schreiber (2021), we employ a sedimentation–diffusion ansatz to model the dependence of the dust velocity dispersion on the diffusivity. The heuristic argument is to compare the settling time under linear gravity at terminal velocity $t_{\text{set}} = 1/(t_s \Omega^2)$ with the diffusion time $t_{\text{diff}} = 1/(D k^2)$ across a length scale $\sim 1/k$, where D is the mass diffusion coefficient of dust. Similar to Brownian motion (Einstein 1905), sedimentation–diffusion equilibrium⁴ leads to $D/t_s = \Omega^2/k^2 \equiv c_d^2$. The regularized expression, which does not diverge in the limit of $\tau_s = 0$, requires consideration of the gas also, leading to a dust layer thickness of $H_d = \sqrt{\delta/(\delta + \tau_s)} H$ (see, e.g., Lin 2021). We define the effective particle velocity dispersion via

$$c_d \equiv \Omega H_d = \sqrt{\frac{\delta}{\delta + \tau_s}} c_s = \sqrt{\frac{D}{D + t_s c_s^2}} c_s. \quad (\text{B1})$$

As also noted by Klahr & Schreiber (2021), the sedimentation–diffusion velocity dispersion c_d , and thus our closure relation, is in general different to the rms velocity of the particles. The Hinze–Tchen formalism for turbulent transport neglecting orbital oscillations or other external forces (Tchen et al. 1947; Hinze et al. 1959), gives the rms velocity as (also see, e.g.,

⁴ Note, that this same argument can be made in the radial direction by replacing the stellar vertical gravity with the restoring force from radial epicyclic oscillations as $-\Omega^2 x$.

Fan & Zhu 1998; Youdin & Lithwick 2007; Binkert 2023)

$$v_{\text{rms}}^2 = \frac{t_c}{t_c + t_s} u_{\text{rms}}^2, \quad (\text{B2})$$




with gas velocity dispersion u_{rms} and correlation time of the turbulence t_c , which connect to the gas diffusivity D_g via $D_g = t_c u_{\text{rms}}^2$. Only if $D_g \sim D$ (see Equation (59)) and $t_s \gg t_c$ does the rms velocity equal the velocity dispersion following from the sedimentation–diffusion ansatz. While the former is fairly well grounded in numerical simulations (e.g., Schreiber & Klahr 2018), the latter is somewhat more ambiguous. For Kolmogorov turbulence, the correlation time equals the turnover time of the largest eddies, which in protoplanetary disks equals Ω^{-1} (Youdin & Lithwick 2007). On the other hand, Schreiber & Klahr (2018) find for simulations values with active streaming instability values of $t_c \sim 0.1\Omega^{-1}$. Indeed, ignoring orbital oscillations is only a good model if t_s and $t_c \ll 1$. For larger particles, epicyclic oscillations are important; particles can decouple from the turbulence and the velocity dispersion and thus diffusion needs to be modified (see Youdin & Lithwick 2007; Youdin 2011; Equation (59)). We neglect this effect in this work. While our pressure term does vanish for large stopping times like the prescriptions used by, e.g., Youdin (2011) and Umurhan et al. (2020), the diffusivity itself does not, and is instead treated as an independent parameter. This is important to be kept in mind when evaluating our model, in particular in the large stopping time limit.

Klahr & Schreiber (2021) call c_d the pseudo–sound speed, which is appropriate as long as c_d is constant. In our work, we allow the diffusivity to depend on density, and thus $c_d^2 \propto D \propto \Sigma^{\beta_{\text{diff}}}$. As a result, the dust pressure takes the form of a polytropic equation of state, i.e., $P_d \propto \Sigma^{1+\beta_{\text{diff}}}$. One can now formally define a dust sound speed a_d via

$$a_d^2 = \frac{\partial P}{\partial \Sigma} \propto (1 + \beta_{\text{diff}}) \Sigma^{\beta_{\text{diff}}}. \quad (\text{B3})$$

If $\beta_D < -1$, this effective squared sound speed is negative, and as a result, so too are the associated pressure perturbations. Indeed, such a negative pressure perturbation is a necessary (but not sufficient) requirement for the diffusion-dependent pressure-driven diffusive instability that may operate for $\tau_s \lesssim 1$, as discussed in this paper.

ORCID iDs

Konstantin Gerbig  <https://orcid.org/0000-0002-4836-1310>
 Min-Kai Lin (林明楷)  <https://orcid.org/0000-0002-8597-4386>
 Marius Lehmann  <https://orcid.org/0000-0002-0496-3539>

References

Bai, X. N., & Stone, J. M. 2010, *ApJL*, 722, L220
 Balbus, S. A., & Hawley, J. F. 1991, *ApJ*, 376, 214
 Ballouz, R. L., Richardson, D. C., & Morishima, R. 2017, *AJ*, 153, 146
 Barker, A. J., & Latter, H. N. 2015, *MNRAS*, 450, 21
 Binkert, F. 2023, *MNRAS*, 525, 4299
 Birmstiel, T., Fang, M., & Johansen, A. 2016, *SSRv*, 205, 41
 Birmstiel, T., Klahr, H., & Ercolano, B. 2012, *A&A*, 539, A148
 Blum, J. 2018, *SSRv*, 214, 52
 Carballido, A., Fromang, S., & Papaloizou, J. 2006, *MNRAS*, 373, 1633
 Carrera, D., Johansen, A., & Davies, M. B. 2015, *A&A*, 579, A43
 Chambers, J. E. 2010, *Icar*, 208, 505

Chen, K., & Lin, M. K. 2020, *ApJ*, 891, 132
 Colwell, J. E., Esposito, L. W., Sremčević, M., Stewart, G. R., & McClintock, W. E. 2007, *Icar*, 190, 127
 Cuzzi, J. N., Dobrovolskis, A. R., & Champney, J. M. 1993, *Icar*, 106, 102
 Dullemond, C. P., & Penzlin, A. B. T. 2018, *A&A*, 609, A50
 Einstein, A. 1905, *AnP*, 322, 549
 Fan, L., & Zhu, C. 1998, *Principles of Gas-Solid Flows* (Cambridge: Cambridge Univ. Press)
 Flock, M., & Mignone, A. 2021, *A&A*, 650, A119
 Flock, M., Nelson, R. P., Turner, N. J., et al. 2017, *ApJ*, 850, 131
 Garaud, P., Barrière-Fouchet, L., & Lin, D. N. C. 2004, *ApJ*, 603, 292
 Gerbig, K., & Li, R. 2023, *ApJ*, 949, 81
 Gerbig, K., Murray-Clay, R. A., Klahr, H., & Baehr, H. 2020, *ApJ*, 895, 91
 Goodman, J., & Pindor, B. 2000, *Icar*, 148, 537
 Harris, C. R., Millman, K. J., van der Walt, S. J., et al. 2020, *Natur*, 585, 357
 Hartlep, T., & Cuzzi, J. N. 2020, *ApJ*, 892, 120
 Hedman, M. M., Nicholson, P. D., & Salo, H. 2014, *AJ*, 148, 15
 Hinze, J. 1959, *Turbulence: An Introduction to Its Mechanism and Theory* (New York: McGraw-Hill)
 Hsu, C. Y., & Lin, M. K. 2022, *ApJ*, 937, 55
 Huang, P., & Bai, X. N. 2022, *ApJS*, 262, 11
 Hunter, J. D. 2007, *CSE*, 9, 90
 Jacquet, E., Balbus, S., & Latter, H. 2011, *MNRAS*, 415, 3591
 Johansen, A., Kato, M., & Sano, T. 2011, in *IAU Symp. 274, Advances in Plasma Astrophysics*, ed. A. Bonanno, E. de Gouveia Dal Pino, & A. G. Kosovichev (Cambridge: Cambridge Univ. Press), 50
 Johansen, A., & Klahr, H. 2005, *ApJ*, 634, 1353
 Johansen, A., Mac Low, M. M., Lacerda, P., & Bizzarro, M. 2015, *SciA*, 1, 1500109
 Johansen, A., & Youdin, A. 2007, *ApJ*, 662, 627
 Johansen, A., Youdin, A., & Mac Low, M. M. 2009, *ApJL*, 704, L75
 Klahr, H., & Hubbard, A. 2014, *ApJ*, 788, 21
 Klahr, H., & Schreiber, A. 2016, in *IAU Symp. 318, Asteroids: New Observations, New Models*, ed. S. R. Chesley et al. (Cambridge: Cambridge Univ. Press), 1
 Klahr, H., & Schreiber, A. 2020, *ApJ*, 901, 54
 Klahr, H., & Schreiber, A. 2021, *ApJ*, 911, 9
 Krapp, L., Benítez-Llambay, P., Gressel, O., & Pessah, M. E. 2019, *ApJL*, 878, L30
 Latter, H. N. 2016, *MNRAS*, 455, 2608
 Latter, H. N., & Ogilvie, G. I. 2006a, *MNRAS*, 372, 1829
 Latter, H. N., & Ogilvie, G. I. 2006b, *Icar*, 184, 498
 Latter, H. N., & Ogilvie, G. I. 2008, *Icar*, 195, 725
 Latter, H. N., & Ogilvie, G. I. 2009, *Icar*, 202, 565
 Latter, H. N., & Ogilvie, G. I. 2010, *Icar*, 210, 318
 Lehmann, M., & Lin, M. K. 2022, *A&A*, 658, A156
 Lehmann, M., & Lin, M. K. 2023, *MNRAS*, 522, 5892
 Lehmann, M., Schmidt, J., & Salo, H. 2017, *ApJ*, 851, 125
 Lehmann, M., Schmidt, J., & Salo, H. 2019, *A&A*, 623, A121
 Li, R., & Youdin, A. N. 2021, *ApJ*, 919, 107
 Li, R., Youdin, A. N., & Simon, J. B. 2018, *ApJ*, 862, 14
 Lin, D. N. C., & Bodenheimer, P. 1981, *ApJL*, 248, L83
 Lin, M. K. 2019, *MNRAS*, 485, 5221
 Lin, M. K. 2021, *ApJ*, 907, 64
 Lin, M. K., & Youdin, A. N. 2015, *ApJ*, 811, 17
 Lin, M. K., & Youdin, A. N. 2017, *ApJ*, 849, 129
 Lyra, W. 2014, *ApJ*, 789, 77
 Mondino-Llermanos, A. E., & Salo, H. 2023, *MNRAS*, 521, 638
 Nelson, R. P., Gressel, O., & Umurhan, O. M. 2013, *MNRAS*, 435, 2610
 Onishi, I. K., & Sekiya, M. 2017, *EP&S*, 69, 50
 Paardekooper, S. J., McNally, C. P., & Lovascio, F. 2020, *MNRAS*, 499, 4223
 Pan, L. 2020, *ApJ*, 898, 8
 Pfeil, T., & Klahr, H. 2021, *ApJ*, 915, 130
 Rein, H., & Latter, H. N. 2013, *MNRAS*, 431, 145
 Riols, A., Lesur, G., & Menard, F. 2020, *A&A*, 639, A95
 Salo, H., & Schmidt, J. 2010, *Icar*, 206, 390
 Salo, H., Schmidt, J., & Spahn, F. 2001, *Icar*, 153, 295
 Sano, T., Miyama, S. M., Umebayashi, T., & Nakano, T. 2000, *ApJ*, 543, 486
 Schäfer, U., Yang, C. C., & Johansen, A. 2017, *A&A*, 597, A69
 Schmidt, J., & Salo, H. 2003, *PhRvL*, 90, 061102
 Schmidt, J., Salo, H., Spahn, F., & Petzschmann, O. 2001, *Icar*, 153, 316
 Schmit, U., & Tscharnuter, W. 1995, *Icar*, 115, 304
 Schmit, U., & Tscharnuter, W. 1999, *Icar*, 138, 173
 Schröpler, R., & Henning, T. 2004, *ApJ*, 614, 960
 Schreiber, A., & Klahr, H. 2018, *ApJ*, 861, 47

- Sekiya, M., & Onishi, I. K. 2018, *ApJ*, 860, 140
- Shakura, N. I., & Sunyaev, R. A. 1973, *A&A*, 24, 337
- Shariff, K., & Cuzzi, J. N. 2011, *ApJ*, 738, 73
- Shibaike, Y., & Alibert, Y. 2020, *A&A*, 644, A81
- Shu, F. H., & Stewart, G. R. 1985, *Icar*, 62, 360
- Spahn, F., Schmidt, J., Petzschmann, O., & Salo, H. 2000, *Icar*, 145, 657
- Squire, J., & Hopkins, P. F. 2018, *MNRAS*, 477, 5011
- Stewart, G. R., Lin, D. N. C., & Bodenheimer, P. 1984, in *Planetary Rings*, ed. R. Greenberg & A. Brahic (Tucson, AZ: Univ. Arizona Press), 447
- Takahashi, S. Z., & Inutsuka, S. i 2014, *ApJ*, 794, 55
- Tchen, C. 1947, *Mean Value and Correlation Problems Connected with the Motion of Small Particles Suspended in a Turbulent Fluid* (Dordrecht: Martinus Nijhoff)
- Thomson, F. S., Marouf, E. A., Tyler, G. L., French, R. G., & Rappoport, N. J. 2007, *GeoRL*, 34, 24203
- Tominaga, R. T., Inutsuka, S. i., & Takahashi, S. Z. 2023, *ApJ*, 953, 60
- Tominaga, R. T., Takahashi, S. Z., & Inutsuka, S. i. 2019, *ApJ*, 881, 53
- Tominaga, R. T., Takahashi, S. Z., & Inutsuka, S. i. 2020, *ApJ*, 900, 182
- Umurhan, O. M., Estrada, P. R., & Cuzzi, J. N. 2020, *ApJ*, 895, 4
- Urpín, V., & Brandenburg, A. 1998, *MNRAS*, 294, 399
- van der Velden, E. 2020, *JOSS*, 5, 2004
- Ward, W. R. 1981, *GeoRL*, 8, 641
- Ward, W. R. 2000, in *Origin of the Earth and Moon*, ed. R. M. Canup, K. Righter et al. (Tucson, AZ: Univ. Arizona Press), 75
- Xu, Z., & Bai, X. N. 2022, *ApJL*, 937, L4
- Yang, C. C., & Johansen, A. 2014, *ApJ*, 792, 86
- Yang, C. C., Johansen, A., & Carrera, D. 2017, *A&A*, 606, A80
- Yang, C. C., Mac Low, M. M., & Johansen, A. 2018, *ApJ*, 868, 27
- Yang, C. C., & Zhu, Z. 2021, *MNRAS*, 508, 5538
- Youdin, A. N. 2011, *ApJ*, 731, 99
- Youdin, A. N., & Goodman, J. 2005, *ApJ*, 620, 459
- Youdin, A. N., & Lithwick, Y. 2007, *Icar*, 192, 588
- Youdin, A. N., & Shu, F. H. 2002, *ApJ*, 580, 494
- Zhu, Z., & Yang, C. C. 2021, *MNRAS*, 501, 467